

# Emissivity and reflection model for calculating unpolarized isotropic water surface-leaving radiance in the infrared. 2: Validation using Fourier transform spectrometers

Nicholas R. Nalli,<sup>1,\*</sup> Peter J. Minnett,<sup>2</sup> Eric Maddy,<sup>1,3</sup> W. Wallace McMillan,<sup>3</sup> and Mitchell D. Goldberg<sup>4</sup>

<sup>1</sup>Perot Systems Government Services, Inc., NOAA/NESDIS/STAR, 5211 Auth Road, Camp Springs, Maryland, USA

<sup>2</sup>University of Miami/RSMAS, 4600 Rickenbacker Causeway, Miami, Florida, USA

<sup>3</sup>University of Maryland Baltimore County, Baltimore, Maryland, USA

<sup>4</sup>NOAA/NESDIS/STAR, 5200 Auth Road, Camp Springs, Maryland, USA

\*Corresponding author: Nick.Nalli@noaa.gov

Received 29 November 2007; revised 23 April 2008; accepted 26 May 2008;  
posted 2 June 2008 (Doc. ID 90178); published 29 August 2008

The surface-leaving radiance model developed in Part I [Appl. Opt. **47**, 3701 (2008)] is validated against an exhaustive set of Fourier transform spectrometer field observations acquired at sea. Unlike prior limited studies, these data include varying all-sky atmospheric conditions (clear, cloudy, and dusty), with regional samples from the tropics, mid-latitudes, and high latitudes. Our analyses show the model to have reduced bias over standard models at emission angles  $\gtrsim 45^\circ$ . © 2008 Optical Society of America

OCIS codes: 010.0280, 010.5620, 280.4991, 280.6780.

## 1. Introduction

Field observations obtained at sea over the past decade from the Marine Atmospheric Emitted Radiance Interferometer (M-AERI) [1,2], a high-accuracy sea-going infrared (IR) Fourier transform spectrometer (FTS), have revealed discrepancies between published IR emissivity model calculations [3,4] and observations at larger observing angles and wind speeds [5]. Measured emissivity spectra obtained by Hanafin and Minnett [5] suggest that the published models underestimate emissivity at observing angles  $\gtrsim 45^\circ$ . The magnitude of the discrepancies between observation and calculation are significant in spectral window regions, reaching as much as 0.4 K

in equivalent brightness temperature in the 800–1000  $\text{cm}^{-1}$  longwave IR (LWIR) window [5].

In Part I [6] of this two-part paper, an alternative model was developed for calculating the IR surface-leaving radiance (SLR; see Appendix A for a list of acronyms frequently used in this paper). While retaining the same degree of simplicity, the methodology differs from previously published models [3,7–17] in that it explicitly sets out to treat *both* the surface emitted and the reflected atmospheric components of SLR in a self-consistent, yet practical, manner. This was achieved by relying on radiative transfer calculations to derive an effective surface emissivity, similar to how emissivity spectra are retrieved from M-AERI hyperspectral measurements.

To assess the accuracy of the model developed in Part I, we turn to the large volume of radiance spectra acquired from the AERI class [1] of surface-based

---

0003-6935/08/254649-23\$15.00/0  
© 2008 Optical Society of America

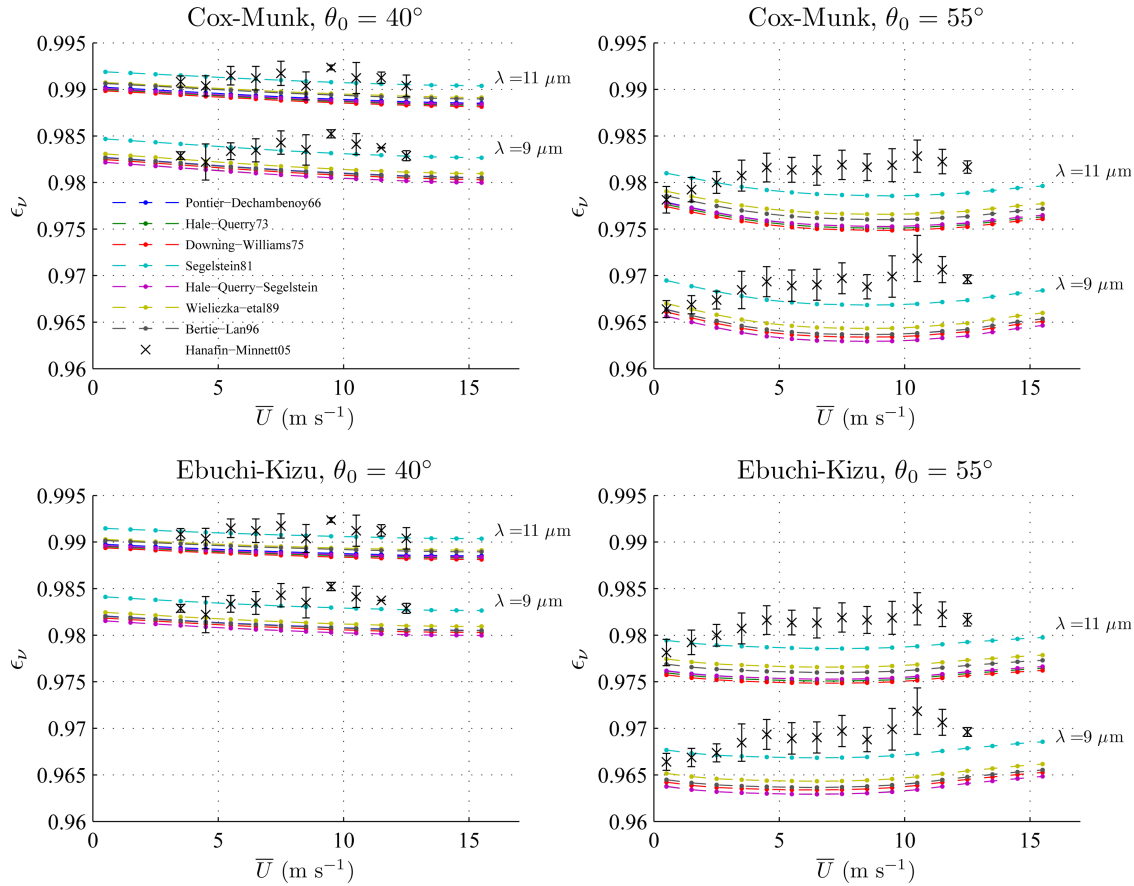


Fig. 1. (Color online) Comparison of modeled sea surface Fresnel emissivities [16] (for the different published  $N_\nu$  as denoted by dashed lines) with the observed emissivities published in Hanafin and Minnett [5] (with  $\times \pm 1\sigma$ ), plotted as functions of surface wind speed for IR wavelengths 11 and 9  $\mu\text{m}$  (see Fig. 15 [5]). Model results in the top plots are based on Cox and Munk [34,35] wave slope PDFs, whereas the bottom plots use Ebuchi and Kizu [36]. The left plots are for  $\theta_0 = 40^\circ$ , the right for  $55^\circ$ . “Hale–Querry–Segelstein” denotes the combination [9] of  $\Re(N_\nu)$  from Hale and Querry [28] and  $\Im(N_\nu)$  from Segelstein [30].

FTS systems over the past ten years. The specific data sets used in this work are overviewed in Section 2. The model is then validated against these data in Sections 3 and 4. These results, along with the simulations in Part I, establish that the new model should attain suitable accuracy for most remote sensing applications.

## 2. Data

M-AERI is a ship-based FTS that measures well-calibrated [18], high-resolution radiance spectra ( $\approx 0.5 \text{ cm}^{-1}$ ,  $\approx 550\text{--}3000 \text{ cm}^{-1}$ ), from both the upwelling and the downwelling directions near the surface [2], usually at a height  $h \lesssim 10 \text{ m}$  above sea level. For more complete technical specifications of the M-AERI instrument, the reader is referred to Minnett *et al.* [2]. The Baltimore–Bomem AERI (BBAERI) is designed after M-AERI, except it is deployed on a stable platform.

The downlooking views from these instruments, measuring upwelling slant path radiances typically at nadir angles  $\theta_0 = 55^\circ$  and  $45^\circ$  for M-AERI and BBAERI, respectively, provide a very close true SLR within window channels (in absorption bands, the atmospheric path between the sensor and the sur-

face contaminates the surface signal). There are also typically two uplooking views measuring downwelling atmospheric radiance,  $I_{\nu a}^\downarrow(\theta)$ : one at the usual  $\theta = 0^\circ$  for boundary layer profiling, and the other at zenith angle  $\theta = \theta_0$  (i.e., the nadir downlooking observing angle is equivalent to the supplement of the zenith uplooking angle). It is the slant path spectra (uplooking and downlooking) that are of direct interest to the present work. For one thing, these measurements allow the retrieval of ocean surface parameters, namely, the surface IR spectral emissivity [1,2,5] along with high accuracy ( $\lesssim 0.1 \text{ K}$  absolute) radiometric sea surface skin temperature (skin SST) [1,2]. It is important to note that the skin SST retrieval from M-AERI or BBAERI is derived in a manner independent of model calculations. By exploiting measurements from a moderately transmissive spectral region ( $\approx 7.7 \mu\text{m}$ ), sensitivity is reduced to variations in the reflected sky radiation component in the sea-viewing measurement that results from the nonunity emissivity [1]. Furthermore, the radiance spectra themselves provide the observations necessary for validating the SLR model developed in Part I.

In addition to the Hanafin and Minnett [5] emissivity observations (results presented in Section 3), we

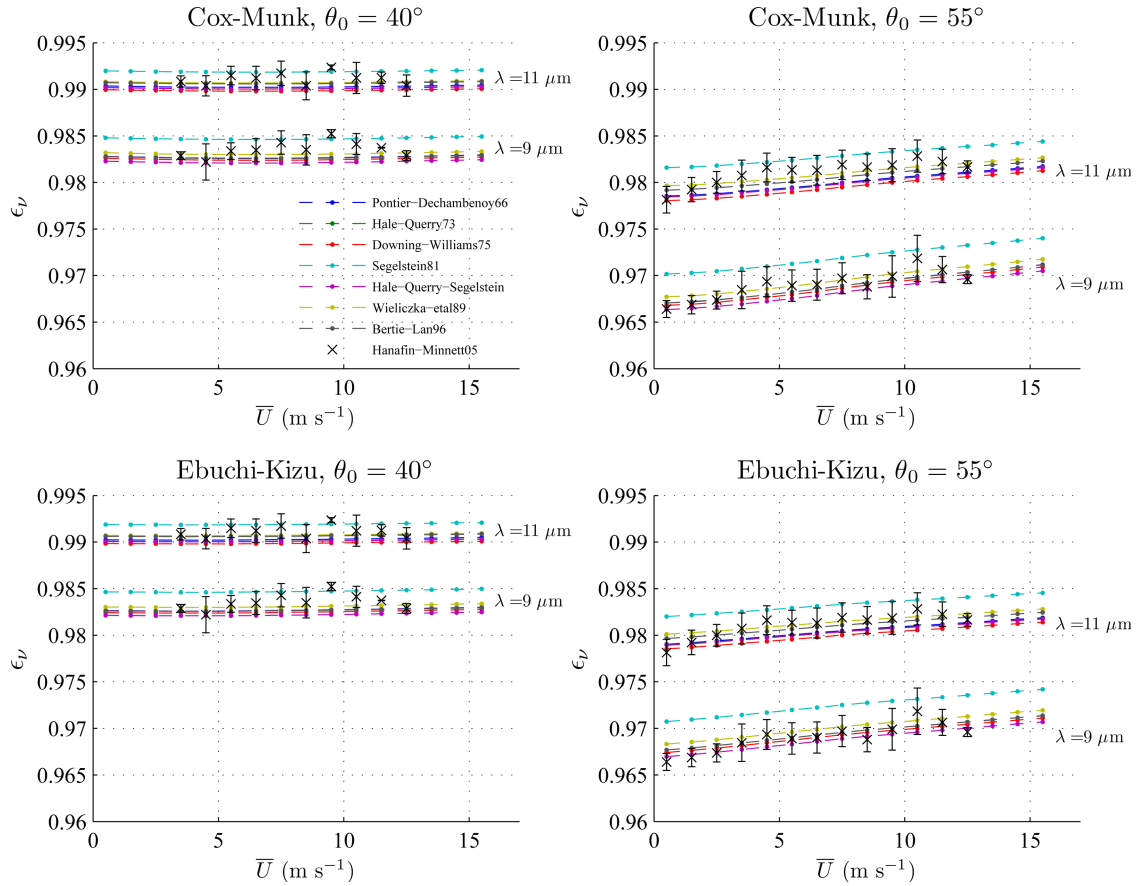


Fig. 2. (Color online) As Fig. 1 except showing the modeled effective emissivity, calculated as  $\epsilon_\nu(\theta_0, \bar{U}_{10}, N_\nu) \equiv 1 - \rho[\Theta_{ie}(\theta'_0, \bar{U}_{10}), N_\nu]$  where  $\Theta_{ie}$  is given in Part I [6], Table 3.

expand the present study in Section 4 to include FTS data acquired at sea from during eight different field campaigns: seven using M-AERI from research vessels and one using BBAERI from a stable platform. The M-AERI data originate from the following cruises (in chronological order): the 1996 Combined Sensor Program (CSP) [19], the 1999 East Atlantic Transect (EAT), the 2001 Asian Pacific Regional Aerosol Characterization Experiment (ACE-Asia) [20], the 2003 Canadian Arctic Shelf Exchange Study (CASES), the 2004 Aerosol and Ocean Science Expedition (AEROSE-I) [21,22], the 2004 Surface-ocean lower-atmosphere studies Air–Sea Gas Exchange Experiment (SAGE) [23], and the 2006 African Monsoon Multidisciplinary Analysis AEROSE-II (AMMA/AEROSE-II) [22]; BBAERI data originate from the AIRS (Atmospheric Infrared Sounder) BBAERI Ocean Validation Experiment (ABOVE), conducted in 2002 and 2003 [24,25]. Each of these field campaigns spanned from a couple to several weeks, with each day containing of the order of  $\simeq 10^2$  individual downlooking and uplooking FTS spectra (details particular to each campaign are provided in Subsection 4.C).

### 3. Emissivity Validation

As described in Part I [6], sea surface emissivity is retrieved operationally from M-AERI spectra by

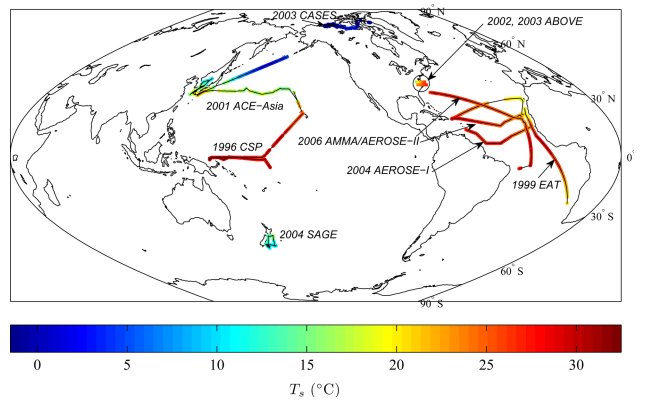


Fig. 3. (Color online) M-AERI and BBAERI retrieved skin SSTs as a function of geographic location for the eight field campaigns used in this study. For plot clarity, only 30% of the M-AERI skin SST retrievals are shown (with the exception of CSP, where the M-AERI prototype configuration sampled SST at about 30% the normal rate). Vessel cruise tracks are shown with solid black lines. The location of the BBAERI at the Chesapeake Lighthouse ( $\simeq 36.9^\circ\text{N}, 75.7^\circ\text{W}$ ) is encompassed by a large circle, with colored bars within the circle showing a statistical summary of the skin SSTs. The 5th, 25th, 50th, 75th, and 95th percentiles for the ABOVE 2002 and 2003 campaign are spread from west to east, and south to north, respectively. Map projection is equal area.

**Table 1. Summary of Field Campaign Samples<sup>a</sup>**

Campaign	$\theta_0$	LWIR Sample (Day + Night)				SWIR Sample (Night Only)			
		N	n	$\bar{U}_{10}$	$\bar{T}_s$	N	n	$\bar{U}_{10}$	$\bar{T}_s$
AEROSE-I	55°	22	2397	8.8	23.4	22	1080	9.2	23.3
AEROSE-II	55°	28	2737	6.0	25.9	28	1198	5.8	26.0
EAT	55°	11	626	3.9	24.0	10	270	3.7	24.2
ACE-Asia	55°	38	4434	6.4	15.5	32	1708	6.3	14.7
SAGE	55°	25	2293	9.4	11.2	24	1066	9.4	11.1
CASES	55°	8	749	7.4	-0.6	8	288	7.4	-0.5
CSP	45°	27	706	6.2	28.9	24	298	6.1	28.8
CSP	55°	27	1396	6.2	28.9	24	594	6.1	28.8
CSP	65°	27	690	6.2	28.9	24	294	6.1	28.8
ABOVE-02	45°	—	—	—	—	13	401	4.4	24.7
ABOVE-03	45°	—	—	—	—	9	241	5.2	22.7

<sup>a</sup>N are the total number of days having data and passing QA, n are the corresponding number of FTS spectra,  $\bar{U}_{10}$  are the mean of daily mean wind speeds at 10 m ( $\text{m s}^{-1}$ ), and  $T_s$  are the mean of daily mean retrieved skin SSTs ( $^\circ\text{C}$ ).

using a VarMinT (minimum temperature variance) algorithm [1,5,26]. More precisely, however, we clarify that the emissivity retrieved by M-AERI [5]

is in fact an *effective* emissivity; that is, it implicitly contains enhancements arising from diffuse reflection.

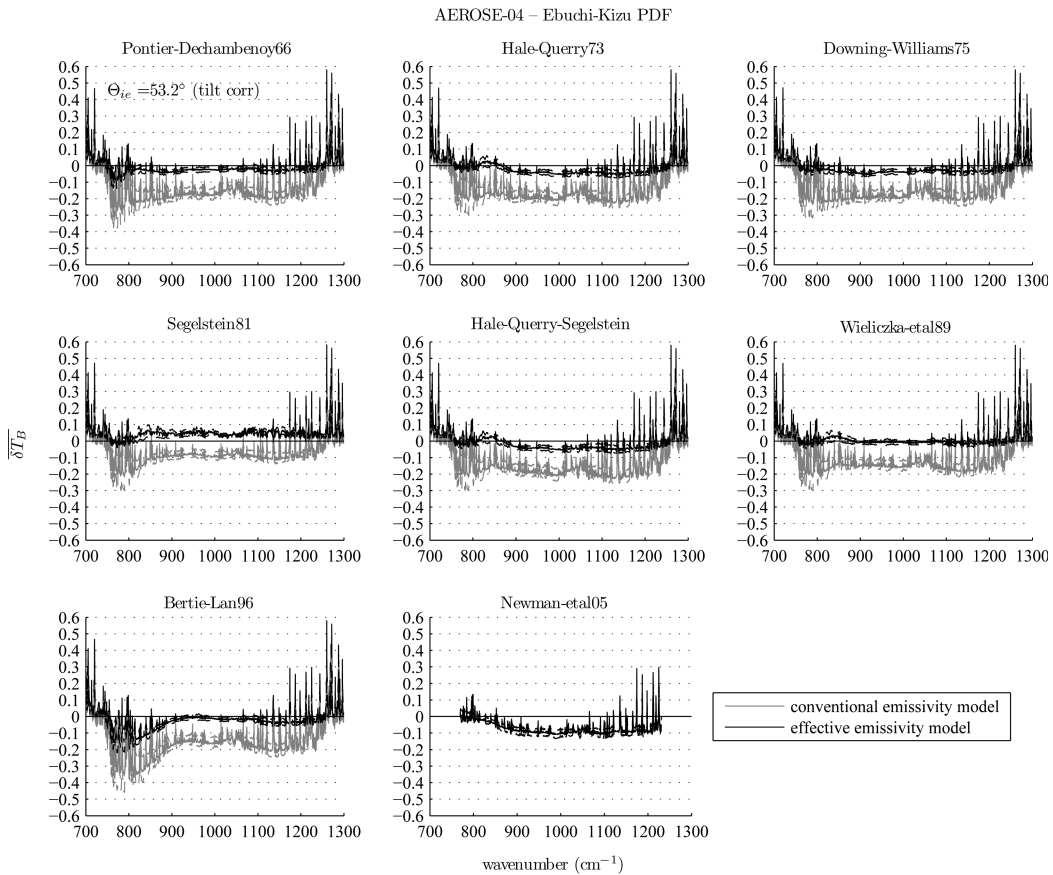


Fig. 4. Mean (solid lines) and interquartile range (IQR; dashed lines) of daily means of SLR calc - obs for the LWIR window region, expressed in apparent brightness temperature difference (K),  $\delta T_B(\nu, \theta_0)$ , defined by Eq. (2) for emission angle  $\theta_0 = 55^\circ$ , from M-AERI during the 2004 AEROSE-I field campaign. The total number of days and M-AERI spectra used in the analysis, along with the mean wind speed and skin SST, are given in Table 2. The gray difference spectra are the result of calculations using a conventional approach outlined in Part I [6], namely, Eq. (3) (with emissivity computed from Eq. (14), after Masuda [16]), whereas the black difference spectra result from using the effective emissivity approach developed in Part I (i.e., Eqs. (7) and (8) [6]). The different panels show the results of using different sets of published optical constants. Shown in the bottom middle plot are results from Part I, Eq. (21), based on the temperature-dependent refractive indices of Newman *et al.* [37], with M-AERI derived daily mean  $\bar{T}_s$  supplying the skin SST input. All calculations utilize the Ebuchi and Kizu [36] isotropic Gaussian wave slope PDF model, and ship roll and pitch data were used to correct for the mean tilt of the vessel from Eq. (1).

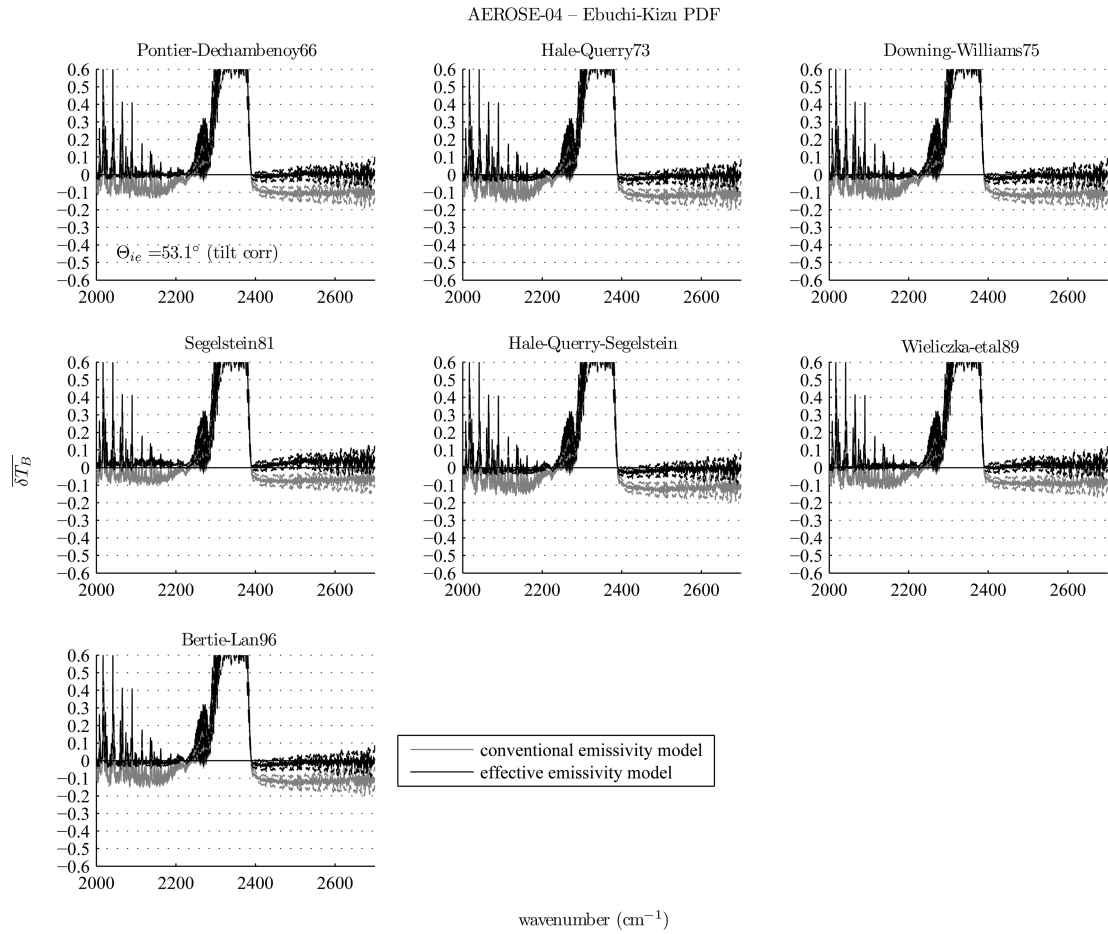


Fig. 5. As in Fig. 4, except for the SWIR window regions during nighttime only. Note that refractive indices from Newman *et al.* [37] are not available at these wavenumbers. The large residuals located between 2230 and 2390  $\text{cm}^{-1}$  are the result of path attenuation between the observer (M-AERI) and the sea surface in the  $\text{CO}_2$  band not accounted for in the models.

Here we revisit the published emissivity data of Hanafin and Minnett [5], specifically, measured spectral emissivities (9 and 11  $\mu\text{m}$ ) at 40° and 55° observing angles, along with coincident surface wind speeds. These measurements were obtained during the 2001 Gas Exchange (GasEx) campaign, which spanned the tropical Pacific Ocean between 4 °S and 16 °N. They analyzed the wind speed dependence of the emissivity measurements and observed an increase with wind speed, most notably at 55° view angle. These were shown in contrast with the modeled values of Masuda *et al.* [3] and Watts *et al.* [4], all of whom predict a decrease with wind speed.

As seen in Fig. 1, we find a similar result from our implementation of Masuda's recently enhanced model [16], Eqs. (20), (21), and (28) of Part I [6], using the two wave slope probability density functions (PDFs) and the various published refractive indices [27–32] (including salinity correction [33]) that we examined in Part I. In light of our work in Part I, this is not surprising, given that Masuda's model [16], as well as other models (e.g., Watts *et al.* [4] and Wu and Smith [9]), rely on very similar formulation (although it is worth noting that we did find Masuda's new model to have slightly better agreement

with M-AERI than that of Wu and Smith). At the 55° angle (right-hand plots), modeled emissivities are seen to decrease to about 8–10  $\text{m s}^{-1}$  before beginning to increase. This change from decreasing to increasing emissivity with wind speed is the result of the modeled surface-emitted, surface-reflected enhancements to emissivity attained from Part I, Eqs. (20) and (21) [4,6,16]. At the 40° angle, modeled emissivities monotonically decrease throughout the measurement range. The end result in both cases is a varying, but systematic, deficit in emissivity for most of the range of wind speeds, with the magnitudes being significant at the 55° observing angle. At  $\lambda = 11 \mu\text{m}$  and  $\bar{U}_{10} = 9.5 \text{ m s}^{-1}$ , assuming the Cox–Munk slope statistics and the Hale–Querry–Segelstein combination of refractive indices [9] (i.e.,  $\Re(N_\nu)$  from Hale and Querry [28] and  $\Im(N_\nu)$  from Segelstein [30]), the model underestimates the measurement by 0.0066, amounting to an equivalent brightness temperature error of  $\delta T_B \simeq -0.445 \text{ K}$  at  $T_s = 298.55 \text{ K}$  (the mean skin SST during the measurement period [5]). It is worth mentioning here that the Wu–Smith model (using Cox–Munk and Hale–Querry–Segelstein) is the basis for the emissivity model parameterizations employed by both the Joint Center

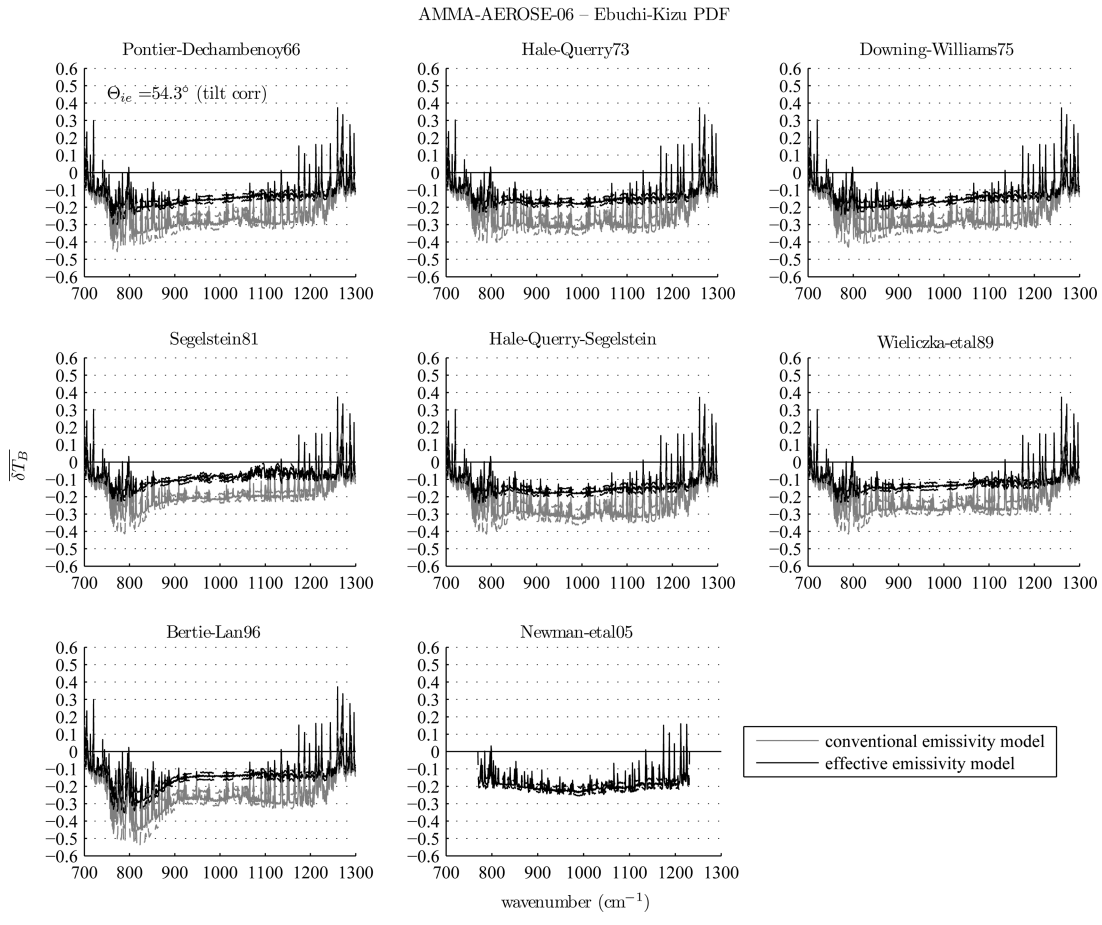


Fig. 6. As in Fig. 4, except from the 2006 AMMA/AEROSE-II field campaign.

for Satellite Data Assimilation Community Radiative Transfer Model (CRTM) and the AIRS product generator executable.

By contrast, plotted in Fig. 2 are the same measurements, but this time shown against calculations obtained from the effective emissivity model developed in Part I [6], namely, through Eqs. (27), (28), (31), and (32). The results show a marked improvement in terms of better overall agreement with the measurements. The results obtained using the Ebuchi-Kizu slope statistics provide a slight improvement over those obtained from using Cox-Munk. We also find that, for these two channels, the Wieliczka *et al.* [31] optical constants yield good agreement with observation (note that we place less confidence in the Segelstein [30] values, given their substantial deviation from the rest of the published data). The majority of the modeled values fall within  $\pm 1\sigma$  of the mean observed values, and the remaining residual deficits are mostly negligible. Because the model does not predict the slight concave-down variation with respect to wind speed, some slight model deficits with respect to these measurements occur in the mid range of wind speeds ( $\approx 4\text{--}11 \text{ m s}^{-1}$ ), with some small surpluses occurring at the lowest wind speeds ( $< 2 \text{ m s}^{-1}$ ) when using the Ebuchi-Kizu statistics. In direct comparison with the above results (i.e.,  $11 \mu\text{m}$  and  $\bar{U}_{10} = 9.5 \text{ m s}^{-1}$ , assuming the same

Cox-Munk slope statistics and “Hale-Querry-Segelstein” refractive indices), the discrepancy with measurement is reduced to 0.0015, resulting in an equivalent brightness temperature deficit of  $\delta T_B \simeq -0.101 \text{ K}$ . If we use instead the Ebuchi-Kizu slope statistics and the Wieliczka *et al.* optical constants, the result is optimized, with the remaining deficit,  $-2.12 \times 10^{-5}$  or  $\delta T_B \simeq -0.001 \text{ K}$ , being well within instrument precision.

#### 4. Surface-Leaving Radiance Validation

While the emissivity comparisons in the previous section demonstrate the effective emissivity model to have better agreement with M-AERI observations than does the standard model, the inclusion of reflected downwelling radiance will make up for some emissivity deficit in terms of the apparent surface brightness temperature. Therefore from here out we conduct analyses in terms of SLR spectra.

##### A. Roll-Pitch Angle Correction

As mentioned in Section 1, M-AERI is typically deployed at sea onboard research vessels. Unfortunately, vessel rotational motions (viz., roll and pitch) have a direct effect on the surface incidence angle of the sensor field of view (FOV). Although our approach of using daily means (described below) mitigates this effect (assuming quasi-random wave

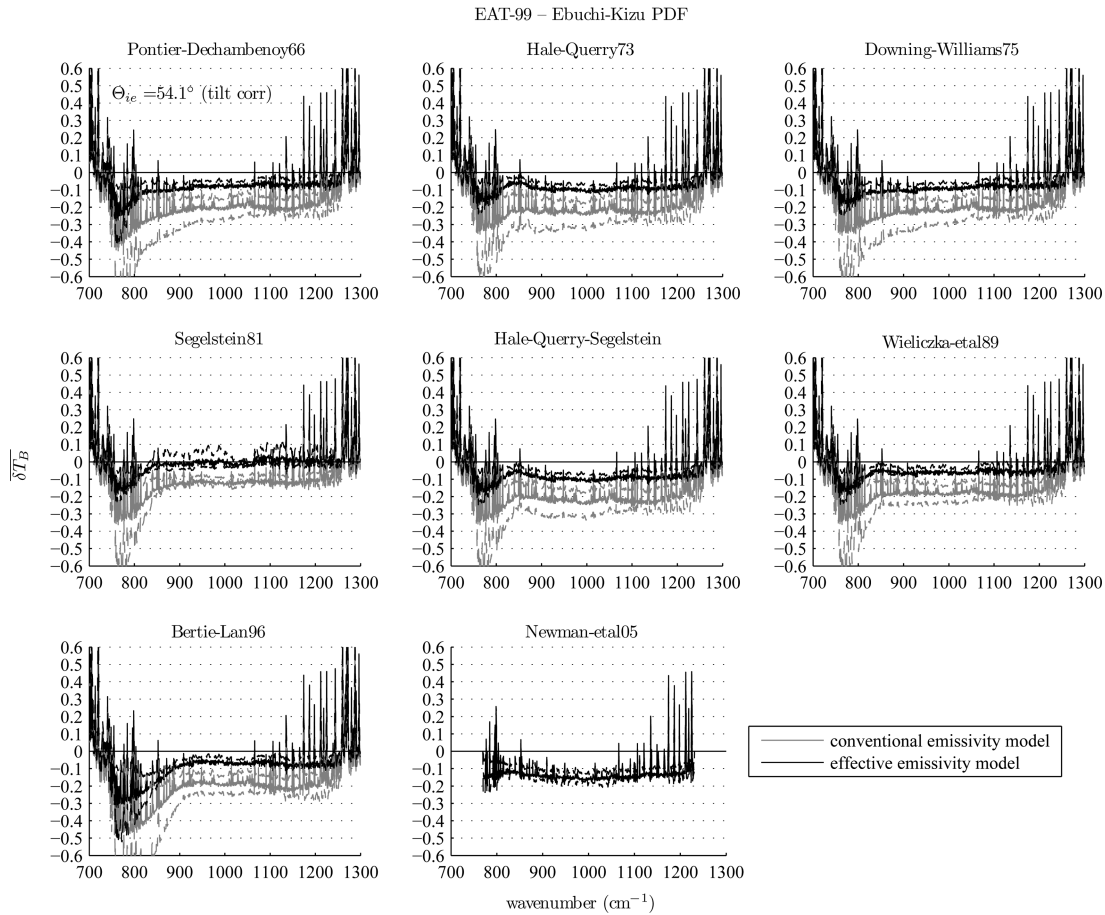


Fig. 7. As in Fig. 4, except from the 1999 EAT field campaign.

motions), the daily mean roll and pitch angles are nonetheless typically nonzero. Therefore, whenever possible for the M-AERI analyses (i.e., when roll and pitch data are available), we attempt to correct for the daily mean tilt of the vessel platform. Assuming the instrument is pointed orthogonal to the longitudinal axis ( $x$  axis) of the vessel, Napier's rules for right spherical triangles may be applied to obtain an expression for the actual incidence angle,  $\theta'_0$ , given the roll and pitch of the vessel,  $\theta_x$  and  $\theta_y$ , respectively:

$$\theta'_0 = \arccos[\cos(\theta_0 - \theta_x) \cos(\theta_y)], \quad (1)$$

where  $\theta_0$  is the known instrument pointing angle. In accordance with roll angle sign conventions,  $\theta_0$  is taken to be negative when the instrument is looking off the port side. In the case of zero roll and pitch,  $\theta'_0$  reduces simply to the instrument pointing angle,  $\theta_0$ . Note that Eq. (1) may also be applied to aircraft-based sensors where Earth curvature is negligible.

#### B. Analysis Procedure

In the subsequent analyses, we quantify the mean spectral calculation minus observation (calc – obs) for each of the field campaigns. To facilitate this, it is convenient to reduce the data volume of each campaign by first computing daily means of all relevant data. This also has the additional benefit of reducing

FTS spectral random noise and colocation uncertainties among the various data sources. As a matter of standard procedure, M-AERI skin temperature data are undergo quality assurance (QA) at the University of Miami before they are approved for research purposes. Here each day of spectra are subject to additional visual QA; days with suspect (e.g., unphysical or noisy) spectra are discarded. Note also that the data used for shortwave IR (SWIR) analyses constitute a nighttime-only subsample of the data (this is necessary to avoid reflected solar contamination). The daily means are then weighted by the number of FTS spectra for the corresponding day to compute the weighted mean calc – obs for each campaign. Daily means of the ancillary data (viz., coincident M-AERI skin SST, surface wind speeds, and vessel roll–pitch) linearly interpolated to the quality-assured M-AERI spectra measurement times are likewise obtained.

We define the daily mean calc – obs in terms of equivalent spectral brightness temperatures as follows:

$$\delta\bar{T}_B(\nu, \theta_0) = B_\nu^{-1}[\bar{R}_\nu^{\text{calc}}(\theta_0)] - B_\nu^{-1}[\bar{R}_\nu^{\text{obs}}(\theta_0)], \quad (2)$$

where  $B_\nu^{-1}$  is the inverse Planck function and  $\bar{R}_\nu^{\text{obs}}(\theta_0)$  is the downlooking ocean-view spectrum measured

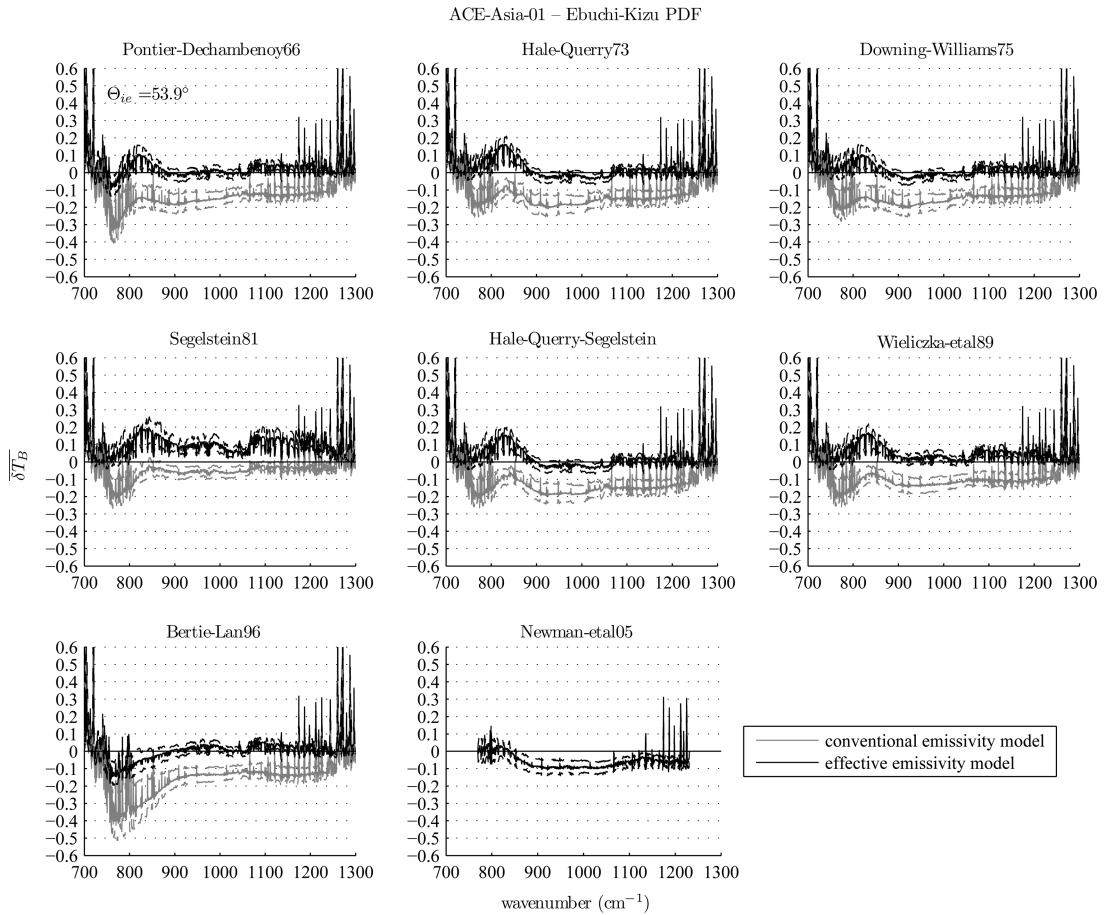


Fig. 8. As in Fig. 4, except from the 2001 ACE-Asia field campaign. Note that a mean tilt correction was not possible owing to the unavailability of ship roll and pitch data.

by either M-AERI or BBAERI, typically at nadir pointing angles  $\theta_0 = 55^\circ$  and  $\theta_0 = 45^\circ$ , respectively; assuming the path absorption and reemission to be negligible,  $\bar{R}_\nu^{\text{obs}}(\theta_0)$  is taken to be the measured SLR. The modeled SLR,  $\bar{R}_\nu^{\text{calc}}(\theta_0)$ , is calculated from

$$\begin{aligned} \bar{R}_\nu^{\text{calc}}(\theta_0) &= \epsilon(\bar{\theta}_0, \bar{U}_{10}, N_\nu) B_\nu(\bar{T}_s) \\ &+ [1 - \epsilon(\bar{\theta}_0, \bar{U}_{10}, N_\nu)] \bar{I}_{\nu a}^l(\theta_0), \end{aligned} \quad (3)$$

where overbars denote daily mean values,  $B_\nu(\bar{T}_s)$  is the Planck blackbody surface emission corresponding to the mean skin SST  $\bar{T}_s$  (retrieved by M-AERI or BBAERI),  $\bar{I}_{\nu a}^l(\theta_0)$  is the M-AERI or BBAERI observed mean downwelling sky radiance at zenith pointing angle  $\theta_0$ , and  $\epsilon(\bar{\theta}_0, \bar{U}_{10}, N_\nu)$  is the modeled spectral emissivity [based on either the conventional approach [16], Part I, Eq. (14) [6], or on our proposed approach, Part I, Eq. (28)] for a given refractive index,  $N_\nu$ , and measured 10 m wind speed,  $\bar{U}_{10}$ . Note that by using the observed downwelling atmospheric radiance,  $\bar{I}_{\nu a}^l(\theta_0)$ , as opposed to a forward calculation based upon a coincident radiosonde [12], analyses based on Eq. (3) can easily include all types of sky condition, including clouds and aerosols, and we also avoid uncertainties arising from errors in radiosonde measurements and forward modeling calculations.

### C. Field Campaign Results

Plotted in Fig. 3 are the M-AERI and BBAERI retrieved skin SSTs as a function of geographic location for the validation field campaigns listed in Section 2. The map illustrates the geographic and thermodynamic sampling ranges, which span the range of conditions typically encountered in practice. Table 1 summarizes the campaign data samples, including the total number of days and FTS spectra, as well as the mean 10 m wind speeds and retrieved skin SSTs. Note that the samples contain more than 150 days of data, amounting to thousands of spectra. To our knowledge, this comprises the most extensive collection of data ever to have been used for this purpose. Given the large data volume, it convenient to discuss the results in the following (nonchronological) order: (1) AEROSE-I and -II and EAT (tropical), (2) ACE-Asia (mid-latitude Spring), SAGE (mid-latitude Autumn) and CASES (polar Autumn), (3) CSP (multiangle, tropical), and (4) ABOVE 2002 and 2003 (stable platform, mid-latitude Summer).

#### 1. AEROSE-I and -II and EAT

The AEROSEs are a series of transatlantic campaigns conducted the onboard the NOAA ship *Ronald H. Brown*, focusing on the tropical Northeast

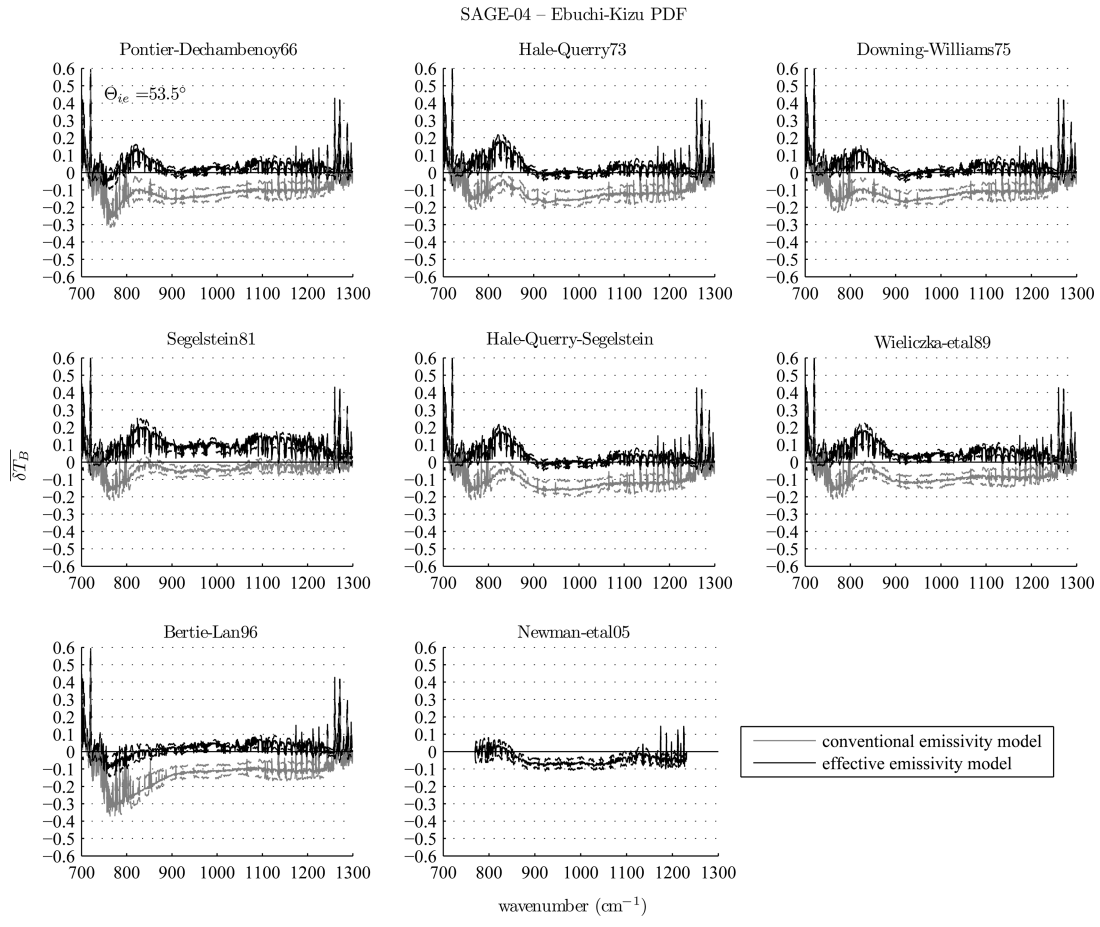


Fig. 9. As in Fig. 8, except from the 2004 SAGE field campaign.

Atlantic [22]. AEROSE-I was conducted during the Northern Hemisphere (NH) Spring (March 2004) and the African Monsoon Multidisciplinary Analysis (AMMA) AEROSE-II piggyback during NH Summer (June–July 2006). Notably, the AEROSE campaigns include a substantial amount of M-AERI spectra obtained during periods of significant outflows of Saharan dust aerosols [21], as well as smoke from biomass burning in sub-Saharan Africa during AMMA/AEROSE-II [22]. The EAT cruise was onboard the German Research Vessel *Polarstern* (Cruise ANT-XVII) during NH Winter (late December 1999 to early January 2000) in the tropical North and South Atlantic. Wind speeds onboard the *Polarstern* are measured at a 39 m mast height, so these are adjusted to an effective 10 m height by using the method outlined in Part I, Appendix B [6]. In all three campaigns, ship roll and pitch data were available to correct for the mean tilt of the vessel by using Eq. (1). The number of days of data,  $N$ , used in the analyses (also given in Table 1) is 22 for AEROSE-I (all days passed QA), 28 for AMMA/AEROSE-II (out of 38), and 11 and 10 for EAT LWIR and SWIR, respectively (all 11 days passed QA, but only 10 had nighttime-only data). The campaign-mean (day + night) wind speeds for AEROSE-I and

-II and EAT are 8.8, 6.0, and 3.9 m s<sup>-1</sup>, respectively (Table 1).

Figures 4 and 5 show the AEROSE-I mean spectra of SLR differences (calc – obs) at emission angle  $\theta_0 = 55^\circ$ , defined by Eq. (2), computed as the mean of daily means, for LWIR and SWIR window regions, respectively. For brevity, here and in the remainder of the paper, we plot only results based on the Ebuchi and Kizu [36] PDF, omitting those based on Cox and Munk [34] (the former model is based on satellite data and appears to yield slightly better agreement with measurements; see Section 3). The individual plots compare results derived by using the different published sets of refractive indices [27–32]. For the LWIR, we also include the results of deriving effective emissivity, Part I, Eq. (28) [6], based on the recently published temperature-dependent refractive indices of Newman *et al.* [37] (Fig. 4 and similar figures, bottom middle plots), who found a significant dependence of the IR optical constants on temperature. Note that the conventional method does not readily lend itself to implementing temperature-dependent indices, given that the required lookup table (LUT), or parametric equation, would need to accommodate the additional skin SST dimension.

Disregarding the obvious large positive deviations resulting from unaccounted path attenuation

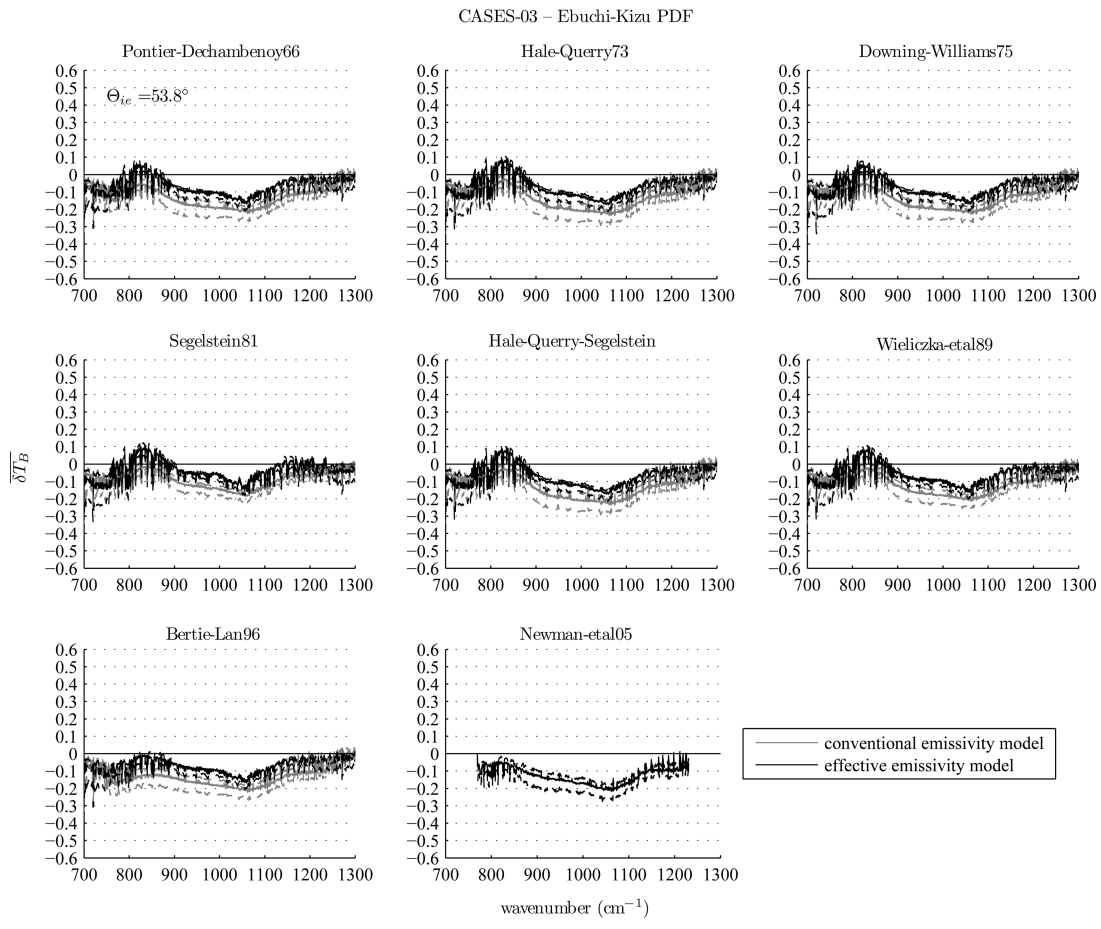


Fig. 10. As in Fig. 8, except from the 2003 CASES field campaign.

between the M-AERI and the surface (primarily within H<sub>2</sub>O lines and the CO<sub>2</sub> and H<sub>2</sub>O absorption bands), the results for the AEROSE-I LWIR (Fig. 4) and SWIR (Fig. 5) are quite similar to those predicted from the tropical atmosphere modeling study in Part I (see Figs. 7 and 10, below, middle plots). An approximate 0.2 and 0.1 K deficit evident in the conventional model (Fig. 5, gray) for the LWIR and SWIR windows (viz.,  $\approx 800\text{--}1000$  and  $1070\text{--}1170\text{ cm}^{-1}$ , and  $2000\text{--}2230$  and  $2400\text{--}2700\text{ cm}^{-1}$ ), respectively, is reduced to well within instrument noise by using the SLR model derived in Part I (black). The AMMA/AEROSE-II results (Fig. 6) show a similar pattern in terms of relative brightness temperature deviations, but for unknown reasons are shifted to negative by  $\approx 0.12$  K in the LWIR and  $\approx 0.1$  K in the SWIR (not shown). The EAT LWIR results (Fig. 7) are, to a lesser degree, also shifted negative by  $\approx 0.05$  K (the SWIR spectra, not shown here, were limited in number and too noisy to ascertain whether they were similarly affected). One possible explanation for these negative shifts would be uncertainties in the instrument pointing angle (and hence, emission angle) arising from ship motions or some other unknown cause. Although ship roll and pitch data were available to estimate the daily mean tilt, the actual mean tilt corrections derived from these data had negligible effect (in fact, the small tilt correction for AMMA/AEROSE-II was actually in the wrong direction). The larger negative biases remaining in AMMA/AEROSE-II may have also resulted from a disturbance of the surface within the M-AERI FOV caused while the *Ronald H. Brown* was holding station (i.e., maintaining a near-zero speed-over-ground) for a large duration of the campaign [22]. When a vessel is under way, the surface FOV of a typical M-AERI configuration (i.e., positioned on a forward upper deck at  $h \approx 9$  m with  $\theta_0 = 55^\circ$ ) is ahead of the bow wave, but the hull of a stationary vessel will sometimes disturb the surrounding surface, with the disturbances possibly propagating out to the FOV. Unaccounted wave slopes within the M-AERI FOV would have the effect of lowering the effective incidence angle and thus increasing the mean emissivity more than that predicted from the wind-speed-based wave slope PDFs. This in turn leads to an underestimation in emissivity, and thus SLR, predicted by the models. There may also be wind-speed measurement errors associated with air flow distortion around the ship's superstructure.

The remaining interesting feature seen in these figures, especially Fig. 7, but not seen in the modeling results in Part I, are the occurrence of pronounced, smoothly varying spectral deviations in

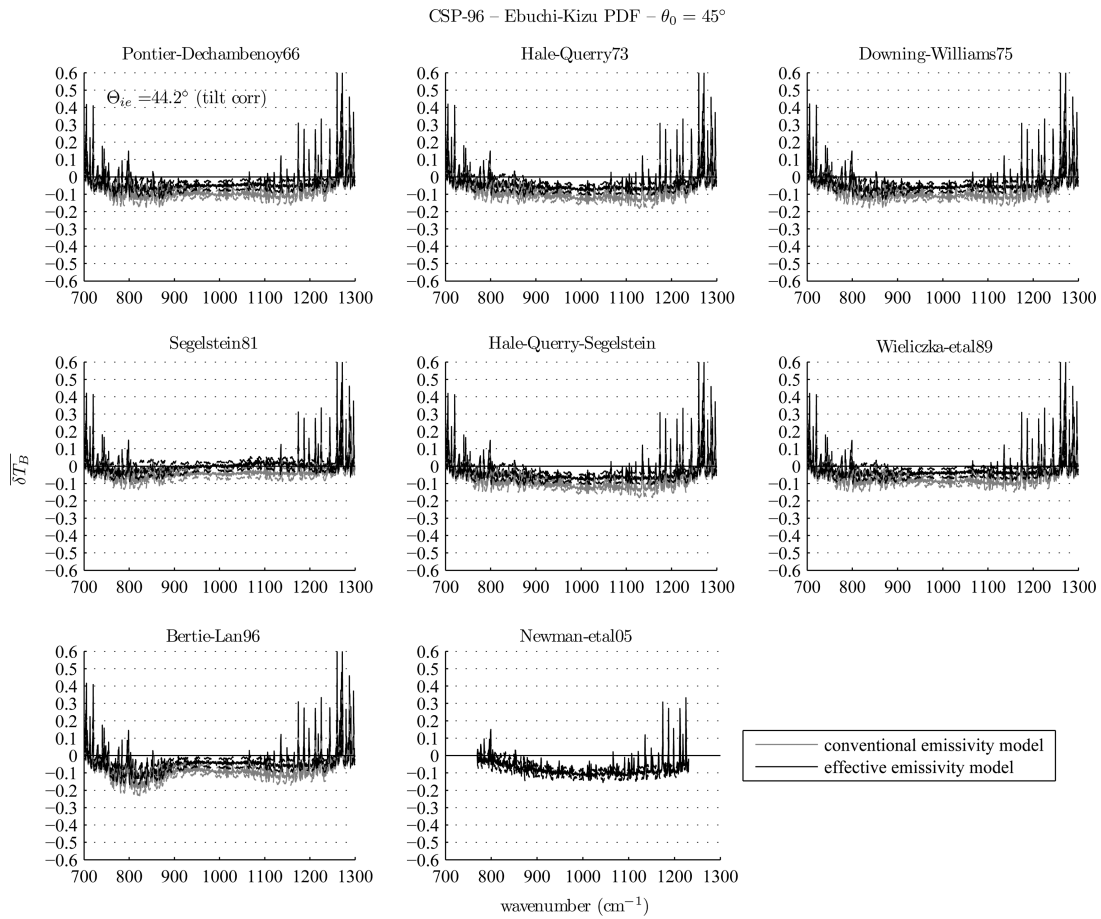


Fig. 11. As in Fig. 4, except for emission angle  $\theta_0 = 45^\circ$  during the 1996 CSP field campaign. Ship roll and pitch data were used to correct for the mean tilt of the vessel from Eq. (1).

the LWIR calc – obs, especially at colder temperatures. These spectral variations are mitigated or exacerbated to different degrees depending on the choice of refractive indices (the Part I modeling studies all assumed perfect knowledge of seawater optical constants). Although some residual atmospheric absorption features were apparent in the Part I simulations (due to the reflectance approximation of the SLR models), these were mostly within instrument noise. We defer a more detailed discussion of the observed calc – obs LWIR spectral features until after all the campaign results have all been presented (Subsection 4.C.5). However, we note that the effective emissivity SLR model not only reduces bias, but here also reduces many spectral artifacts, most notably the water vapor lines and O<sub>3</sub> absorption band ( $\simeq 1000\text{--}1100\text{ cm}^{-1}$ ). Both models appear to have some difficulty capturing the spectral variation of SLR in the vicinity of 750–850 cm<sup>-1</sup> (900 cm<sup>-1</sup> for the Bertie and Lan [32] data set). Possible reasons for this are considered in the discussion in Subsection 4.C.5. Regarding the SWIR, we found the results to show little spectral variation among the different refractive indices (Fig. 5, for example); therefore, in the interest of brevity, we refrain from showing the SWIR spectral plots for every campaign, but rather

summarize the spectral mean results later in Subsection 4.D (Tables 1–5).

## 2. ACE-Asia, SAGE, and CASES

The ACE-Asia was a large-scale field campaign that included shipboard measurements from the *Ronald H. Brown* [20] over the midlatitude Pacific Ocean during NH Spring (mid-March through April 2001). Some of these measurements were obtained during a significant Asian dust outflow event [20]. The 2004 SAGE was conducted onboard the New Zealand National Institute of Water and Atmospheric Research research vessel *Tangaroa* in the South Pacific Ocean off the east coast of New Zealand during the Southern Hemisphere Autumn (mid-March to mid-April 2004) [23]. The 2003 CASES was conducted onboard the Canadian Coast Guard ship *Amundsen* in the Amundsen Gulf during NH Autumn (mid-September to mid-October 2003). During ACE-Asia, the skin SSTs ranged between  $\simeq 2^\circ\text{C}$  and  $24^\circ\text{C}$ , staying mostly within  $10^\circ\text{C}\text{--}20^\circ\text{C}$ , and the campaign-mean wind speed  $\bar{U}_{10} = 6.4\text{ m s}^{-1}$ ; during SAGE,  $T_s$  ranged between  $10^\circ\text{C}$  and  $16^\circ\text{C}$ , mostly within  $10^\circ\text{C}\text{--}12^\circ\text{C}$ , with  $\bar{U}_{10} = 9.4\text{ m s}^{-1}$ ; and during CASES  $T_s$  never exceeded  $5^\circ\text{C}$ , but hovered near the freezing point of seawater ( $-1.9^\circ\text{C}$ ) the majority of

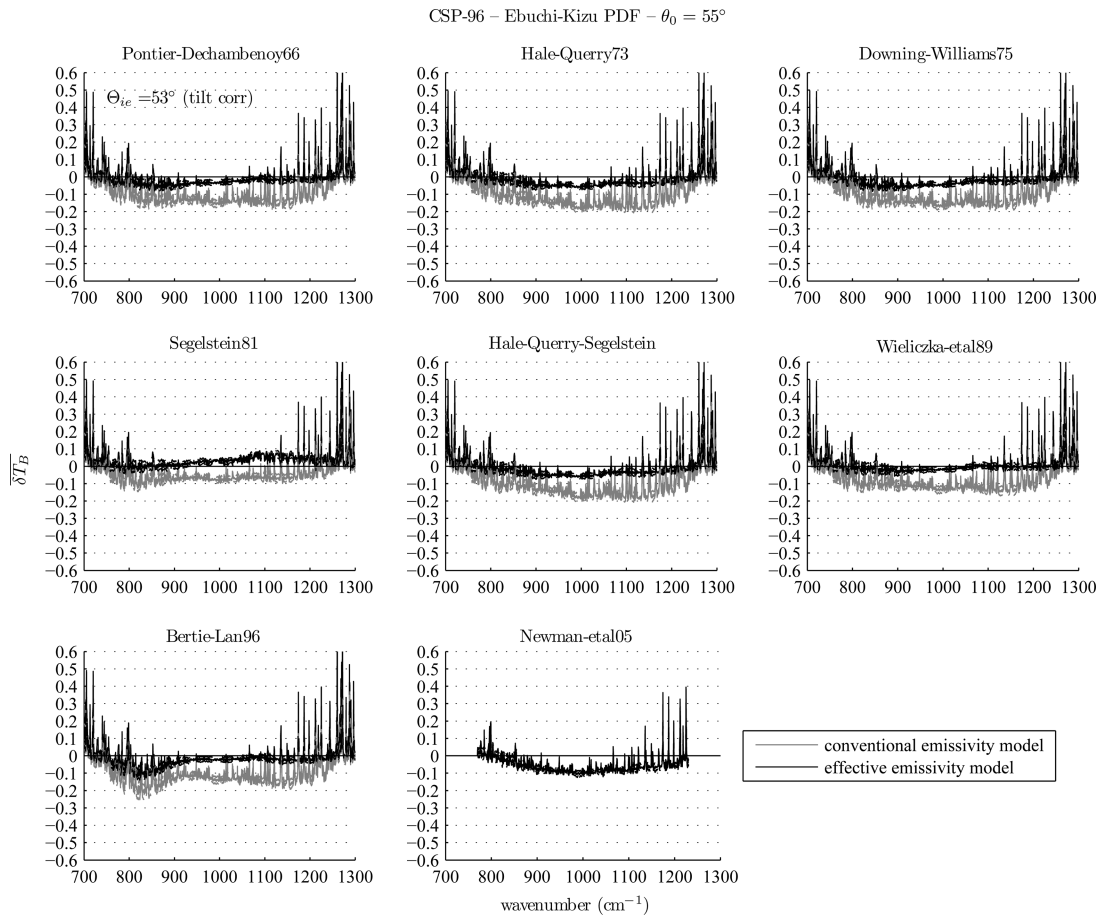


Fig. 12. As in Fig. 11, except for emission angle  $\theta_0 = 55^\circ$ .

the time (spectra with  $T_s \leq -1.9^\circ\text{C}$  were omitted), with  $\bar{U}_{10} = 7.4 \text{ m s}^{-1}$ . Unfortunately, ship roll and pitch data were not readily available for a mean tilt correction in any of these three campaigns.

Figures 8–10 show the mean spectral LWIR SLR difference (calc – obs,  $\theta_0 = 55^\circ$ ) for the ACE-Asia, SAGE, and CASES cruises, respectively. The results for ACE-Asia ( $N = 38$  out of 41 days passing QA, with 32 days having nighttime-only data) and SAGE (all 25 days passing QA, with 24 having nighttime-only data) show a large degree of similarity, both in terms of spectral variability and in absolute magnitudes. This may be expected given the somewhat similar range of surface temperatures during these campaigns. The conventional model bias ranges approximately between  $-0.2$  and  $-0.1 \text{ K}$  in the LWIR (somewhat less than the tropical cases) and  $\approx -0.1 \text{ K}$  in the SWIR (not shown). Although there are some small residual artifacts associated with atmospheric absorption features (viz.,  $\text{H}_2\text{O}$  lines and the  $\text{O}_3$  absorption band) introduced into some of the new model's calc – obs spectra (depending on the published refractive index), it nevertheless again exhibits near-zero mean spectral bias. The CASES results (Fig. 10) exhibit similar, but more extreme, spectral features ( $N = 8$  out of 8 days passing QA). The environmental conditions encountered during CASES re-

present a thermodynamic limiting case, given the polar (cold and dry) atmosphere and near-freezing skin temperatures. In terms of satellite IR remote sensing, such conditions are expected to account for a relatively small fraction of cases [38], and it is quite possible that these cases may end up flagged as ice contaminated or cloudy within operational retrieval algorithms [39]. Furthermore, inspection of the individual atmospheric spectra indicate highly variable sky conditions over the course of each day, especially low-level overcast clouds at or near the surface temperatures intermixed with noncloudy conditions. When the downwelling atmospheric radiance in windows approaches  $B_\nu(T_s)$ , as is the case for opaque clouds with emission temperature  $\simeq T_s$ , the two SLR models will converge to  $B_\nu(T_s)$ , as indicated by Part I, Eqs. (3) and (27) [6], and seen, for example, in the SWIR  $\text{CO}_2$  absorption band (e.g., Part I, Figs. 11–13). As a result of the mixed sky conditions, the improvement in daily mean bias with the new model is less pronounced than with other campaigns, but evident nonetheless. The observed spectral variations are suspected to result primarily from the temperature dependence of the refractive index of water (discussed more in Subsection 4.C.5), or possibly even from the presence of ice, although the presence of opaque clouds has masked this somewhat.

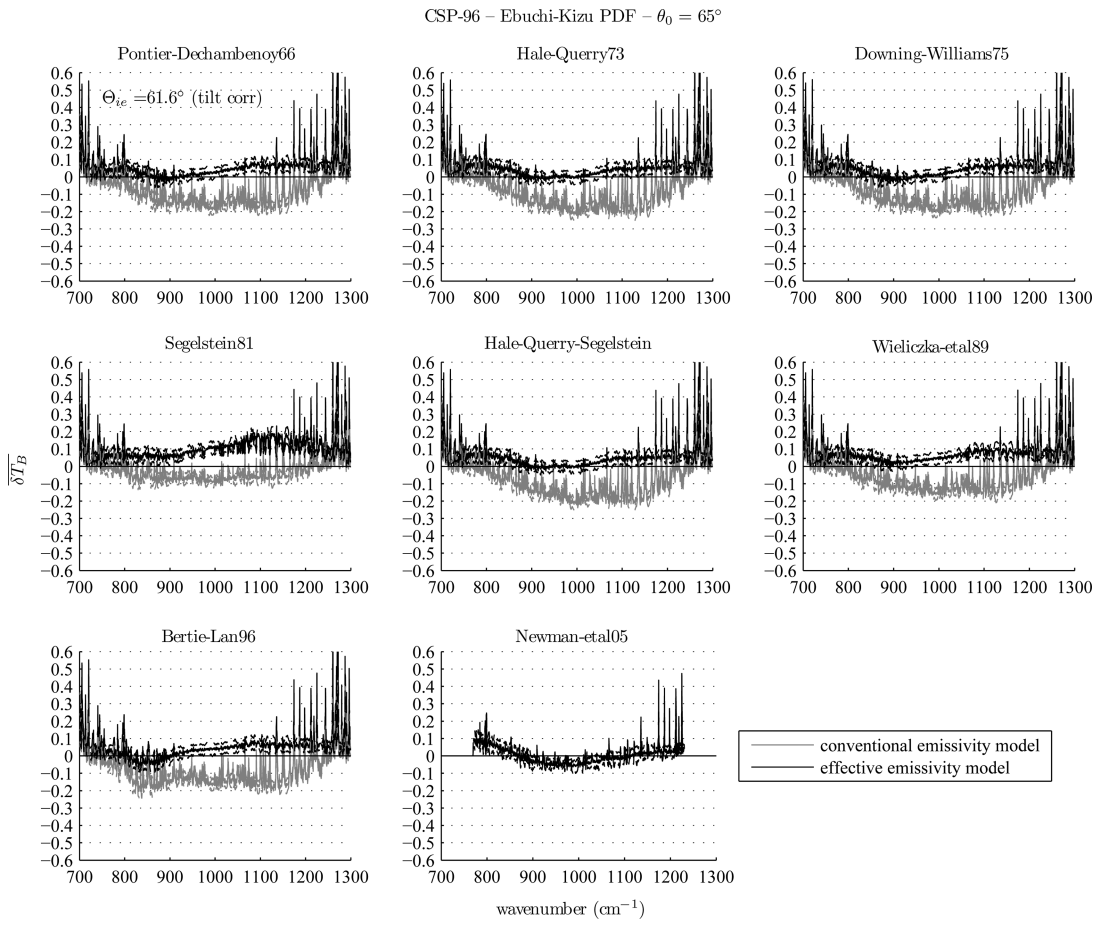


Fig. 13. As in Fig. 11, except for emission angle  $\theta_0 = 65^\circ$ .

### 3. Combined Sensor Program

To test the models against varying emission angles, we turn to the data collected during the 1996 CSP [19]. CSP was a multi-institutional field experiment spanning a 30 day period (14 March to 13 April 1996) in the tropical Pacific onboard the NOAA ship *Discoverer*. Among other things, CSP included the maiden voyage of the M-AERI, and the ensuing data set is unique because of the experimental multiangle scanning at zenith and nadir angles of  $35^\circ$ ,  $45^\circ$ ,  $55^\circ$ ,  $65^\circ$ , and  $75^\circ$  (as well as the usual  $0^\circ$  zenith angle for atmospheric profiling). M-AERI instruments have subsequently been programmed to scan only at  $55^\circ$ , as this was determined to be an optimal angle for downlooking views (it is the smallest angle with a surface FOV located comfortably outside ship wakes) [2]. The *Discoverer* spent a large portion of the cruise sampling within the tropical western Pacific Ocean warm pool, where skin SSTs hovered at or above the  $30^\circ\text{C}$  mark for more than half the sampling duration and the campaign median daily mean wind speed was  $5.7 \text{ m s}^{-1}$ .

We limit our analysis to the three intermediate angles (the  $35^\circ$  angle is within the range where the models largely agree, and the  $75^\circ$  angle is outside the range of validity of the new model). Ship roll

and pitch data were available to correct for the mean tilt of the vessel using Eq. (1). M-AERI LWIR spectra from all 28 CSP days passed QA, but 1 day lacked roll-pitch data and was subsequently omitted ( $N = 27$ ), and three additional days lacked sufficient SWIR nighttime-only data ( $N = 24$ ). Note that M-AERI was programmed to sample the  $55^\circ$  scan angle twice as frequently as the other angles.

Figures 11–13 and 14–16 show the mean CSP surface-leaving radiance calc – obs for LWIR and SWIR window regions and emission angles  $\theta_0 = \{45^\circ, 55^\circ, 65^\circ\}$ , respectively (given the unique multiangle measurements, we show both LWIR and SWIR results). We here direct our attention to the variation of results with respect to emission angle.

At  $\theta_0 = 45^\circ$  (Figs. 11 and 14), the new model offers only a slight reduction in bias (the two models also converge further to a bias of  $\simeq -0.1 \text{ K}$  at the  $35^\circ$  angle, in both the LWIR and SWIR). In Part I it was shown from modeling experiments that the two models are expected to converge at the smaller angles ( $\lesssim 40^\circ$ ), but not to a negative bias. The most plausible explanation would be the effect of the vessel wake on the wave slopes of the M-AERI FOV, which would be located considerably closer to the ship at these smaller emission angles. As conjectured above (i.e., the AMMA/AEROSE-II results in Subsection 4.C.1),

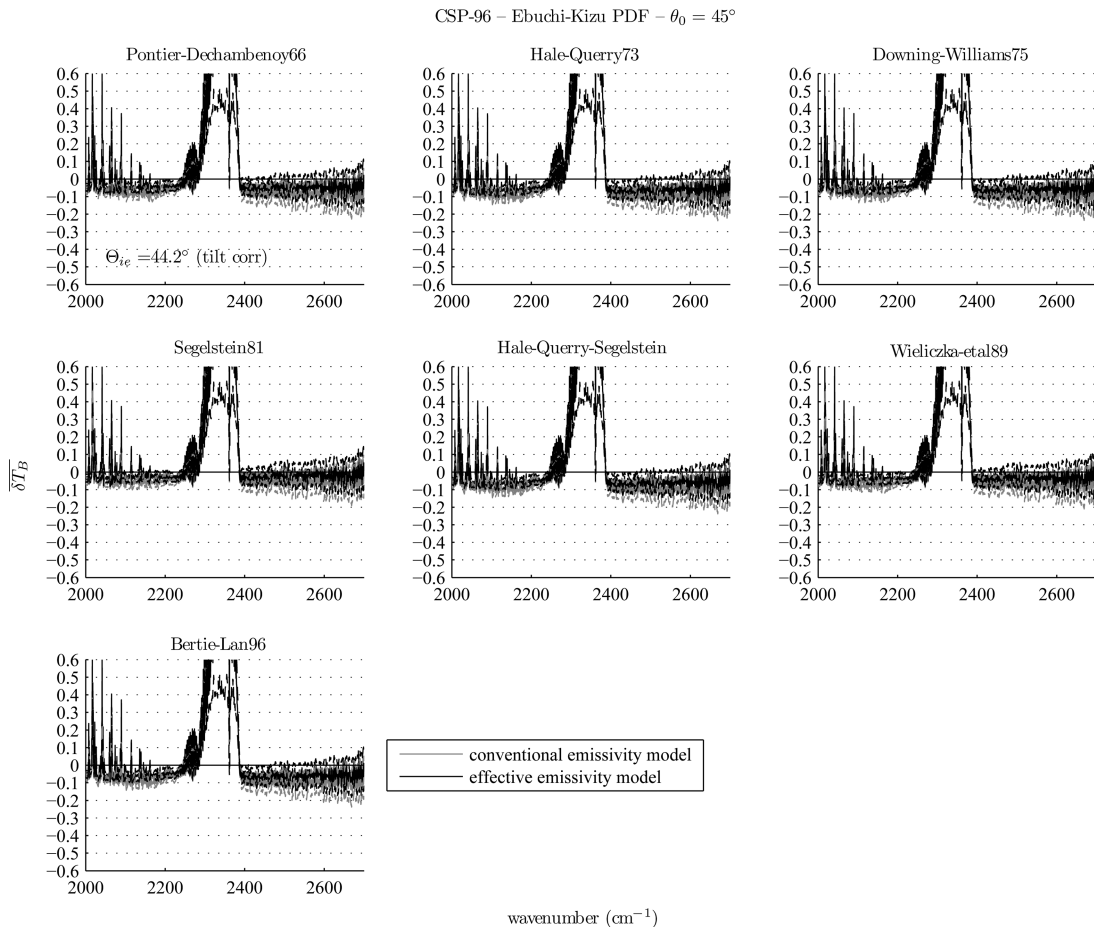


Fig. 14. As in Fig. 11, except for the SWIR window regions during nighttime only; note that refractive indices from Newman *et al.* [37] are not available at these wavenumbers. The large residuals located between  $2230$  and  $2390\text{ cm}^{-1}$  are the result of path attenuation between the observer (M-AERI) and the sea surface in the  $\text{CO}_2$  band not accounted for in the models.

unaccounted wave slopes could lead to an underestimation in SLR by the models.

At  $\theta_0 = 55^\circ$  (Figs. 12 and 15), the conventional model demonstrates negative bias of the same order as shown previously (i.e., in Part I and above), roughly ranging between  $-0.2$  and  $-0.1\text{ K}$  in the LWIR ( $-0.13$  and  $-0.05\text{ K}$  in the SWIR), with the new model significantly reducing this to near zero (depending on the refractive index and spectral region, and excluding the Newman *et al.* [37] temperature-dependent indices; see Subsection 4.C.5).

At  $\theta_0 = 65^\circ$  (Figs. 13 and 16), the magnitude of negative bias in the conventional model varies between  $0.1$  and  $0.2\text{ K}$  in the LWIR (disregarding the path attenuation in the  $\text{H}_2\text{O}$  continuum and  $\text{CO}_2$  absorption regions,  $\nu \lesssim 850\text{ cm}^{-1}$  and  $\nu \gtrsim 1200\text{ cm}^{-1}$ ) and varies between  $0.15$  and  $0.05\text{ K}$  in the SWIR. The new model again significantly reduces the negative bias to near zero, although a small positive bias begins to emerge (depending on the refractive index), especially in the SWIR channels  $>2400\text{ cm}^{-1}$ . The introduction of small positive bias at larger angles was predicted in the modeling study in Part I, albeit of lesser magnitude and/or at  $>65^\circ$  (see Figs. 8 and 11 [6], bottom plots).

#### 4. AIRS BBAERI Ocean Validation Experiment

As already stated, one of the sources of uncertainty in the M-AERI analyses concerns the uncertainty of the surface incidence angle arising from a moving vessel with time-varying pitch and roll. Although we attempted to correct for this effect when pitch and roll data were available, it is nevertheless desirable to allay this uncertainty by supplementing the analyses with data obtained from a stable platform. The ABOVE [24] provides just such a data set.

The ABOVE campaign was carried out during the NH Summers 2002 (during intermittent periods from mid-August to early October) and 2003 (June to early July). BBAERI obtained measurements of uplooking and downlooking IR spectra at  $\theta_0 = \theta'_0 = 45^\circ$  from  $\approx 23\text{ m}$  above mean sea level while deployed at the CERES Ocean Validation Experiment (COVE) [25] site. The COVE site is located at the Chesapeake Lighthouse platform, which is approximately 25 km off the U.S. coast of Virginia ( $36.905^\circ\text{N}$ ,  $75.713^\circ\text{W}$ ). Based on our modeling studies in Part I, the  $45^\circ$  emission angle is where the two SLR models begin to diverge, and given the low to moderate mean wind speeds ( $4.4$  and  $5.2\text{ m s}^{-1}$  for 2002 and 2003, respectively), it can be expected that the differences

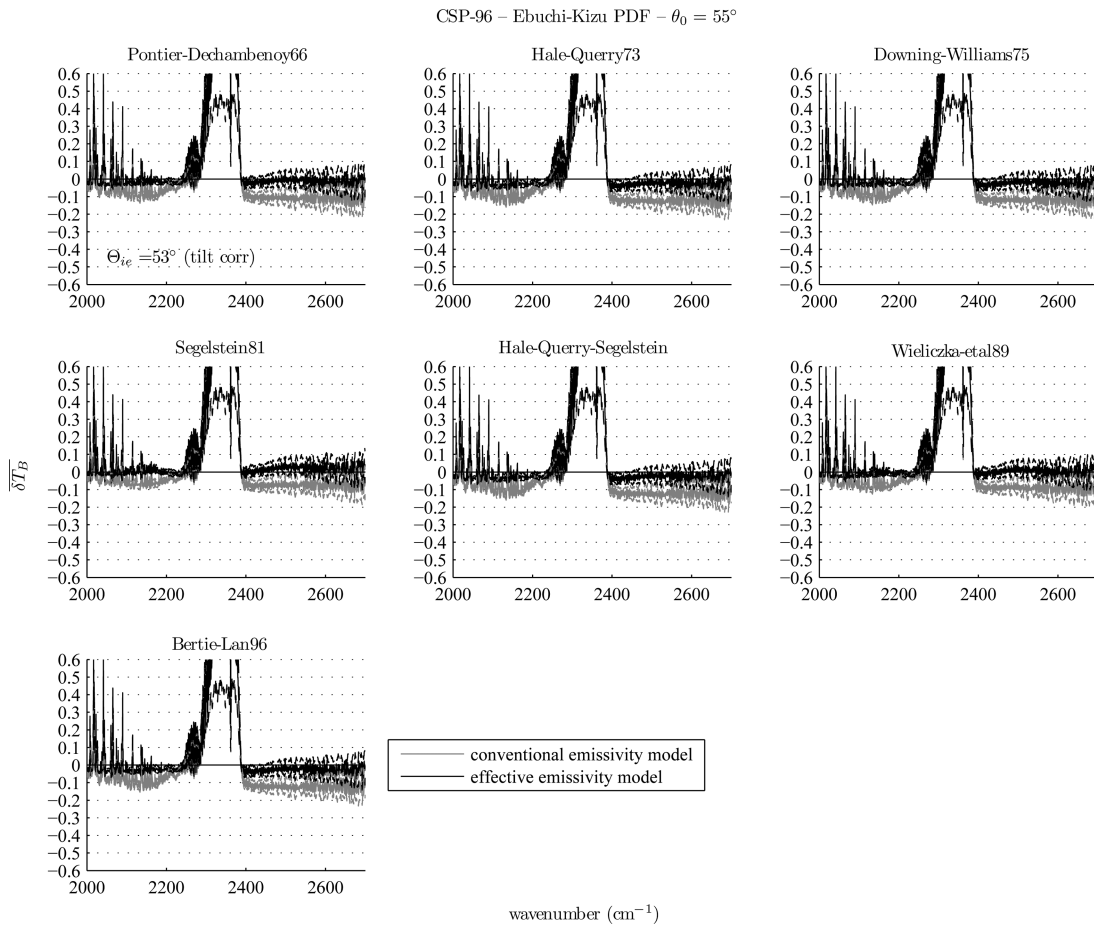


Fig. 15. As in Fig. 12, except for the SWIR window regions during nighttime only.

between the model calculations will be relatively small, albeit still discernible. The anemometer height on the Chesapeake Lighthouse is 43.3 m, so the wind speed measurements require an adjustment to an effective 10 m height by the method outlined in Part I, Appendix B [6]. Finally, it is not likely that the support pylons would disturb the surface wave slope geometry in any appreciable way, especially at the location of BBAERI's surface FOV (approximately 23 m from the pylons).

Because of the relatively high placement of BBAERI above the surface, path absorption and emission will be more pronounced in the LWIR windows owing to nonnegligible  $H_2O$  continuum absorption. Assuming a typical 9 m research vessel deck height and  $55^\circ$  M-AERI pointing angle, the path length for the BBAERI ABOVE configuration is more than double that of M-AERI. Fortunately, however, path absorption and emission can be minimized by restricting ourselves to the supertransparent SWIR window regions. Using the Line-by-Line Radiative Transfer Model version 9.4 [40], we estimate the error arising from assuming unit transmittance (zero absorption and emission) between a downlooking ( $\theta'_0 = 45^\circ$ ) detector at 25 m and the surface to be  $\lesssim | -0.03 |$  K in the SWIR microwindows, even when an  $\approx 1.3$  K inversion is present between the sensor and

the surface (an inversion causes enhanced reflected downwelling; see Subsection 4.C.5). Thus, to avoid uncertainties arising from path absorption and emission, we present only results for the SWIR window regions from the ABOVE campaign.

Before continuing further, we must address another issue pertaining to the height of BBAERI at the COVE site, namely, biases in the retrieved skin SST caused by a relatively thick ( $\approx 32.5$  m slant path), nonisothermal layer between the instrument and the surface. Specifically, it was discovered that during the ABOVE campaign, primarily in 2003, significant temperature inversions (with magnitudes as large as  $\approx 5$  K) had occurred in the surface layer, especially, but not exclusively, prior to UTC decimal hour 0.5 (i.e., from 19:00 to 07:00 LST). The BBAERI  $T_s$  retrieval, necessary for the SLR calculation, Eq. (3), requires an *a priori* surface air temperature, which is estimated simply as the mean of 43 channels located between  $670$  and  $690$   $cm^{-1}$  of the  $CO_2$  region. This estimate,  $T_{sa}^{CO_2}$ , corresponds to the emission temperature of a path no more than 10 m in length, but is assumed to represent the air temperature of the entire lowest layer (put another way, the layer from the surface up to the BBAERI level is assumed to be isothermal). However, if the temperature within this layer varies appreciably,  $T_{sa}^{CO_2}$  will not be

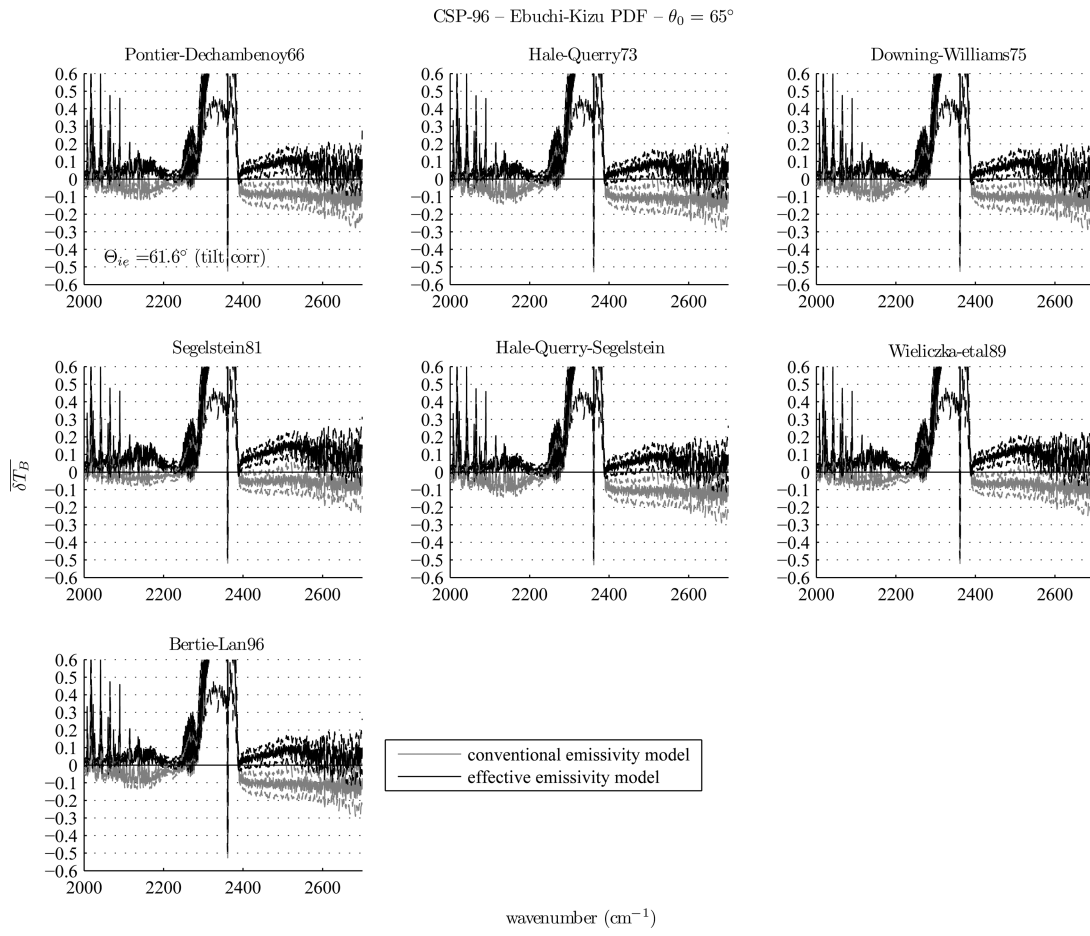


Fig. 16. As in Fig. 13, except for the SWIR window regions during nighttime only.

representative of the lowest layer temperature, ultimately leading to errors in the retrieved  $T_s$ . The sensitivity of the  $T_s$  retrieval to perturbations in the surface layer temperature,  $T_{sa}$  was investigated by using radiative transfer simulations (derived from the UMBC\_LBL version 7 transmittance model). It was found that the resulting errors in retrieved  $T_s$  corresponded roughly to  $\delta T_s \approx -0.1\delta T_{sa}$  (within the range  $-3 \leq \delta T_{sa} \leq 3$  K). In the case of a temperature inversion, the layer temperature is biased cold relative to the *a priori* temperature,  $T_{sa}^{\text{CO}_2}$ , and thus a positive skin SST error results. To avoid these erroneous cases in our analyses, daily mean spectra with CO<sub>2</sub> band (2250–2400 cm<sup>-1</sup>) emissions surpassing those in the adjacent window regions by 1 K or more are discarded. This entailed only 1 day out of 16 in 2002, with 2 days missing nighttime-only data, leaving  $N = 13$  days; however in 2003, a majority of days were found to exhibit these conditions (25 out of 34), leaving  $N = 9$  days for analysis.

Figures 17 and 18 show the mean calc – obs for the ABOVE campaign, Summers 2002 and 2003, respectively. While the differences between the two models are small (as expected, given the observing angle  $\theta'_0 = 45^\circ$ ), they are nevertheless consistent with those predicted in the modeling studies in Part I, Figs. 11–13 [6], with the new model minimizing

any residual bias. Furthermore, because these spectra were obtained from a stable platform causing only minimal disturbance of the surface, we gain more confidence in both models for this particular viewing angle. Recall that the CSP results at 45° show both models with a small negative bias (Figs. 11 and 14). The ABOVE results thus reinforce our speculation that the CSP biases probably resulted from FOV contamination by the ship wake. As a final note, unlike the results from the M-AERI campaigns, the interquartile range (IQR) in the CO<sub>2</sub> absorption band ( $\approx 1.1$  K) is nearly symmetrical about zero. The lower (negative) quartile is the result of cases with surface layer temperature inversions passing QA.

## 5. Spectral Variations

As mentioned above in Subsection 4.C.1, residual spectral variations in the LWIR calc – obs warrant further discussion. Such spectral variations were not observed in the modeling studies in Part I, which, among other things, assumed perfect knowledge of the seawater  $N$ , and no intervening atmosphere between the sensor and surface. Most of these spectral features are believed to be the direct result of either one, or both, of these assumptions breaking down under certain circumstances encountered in the

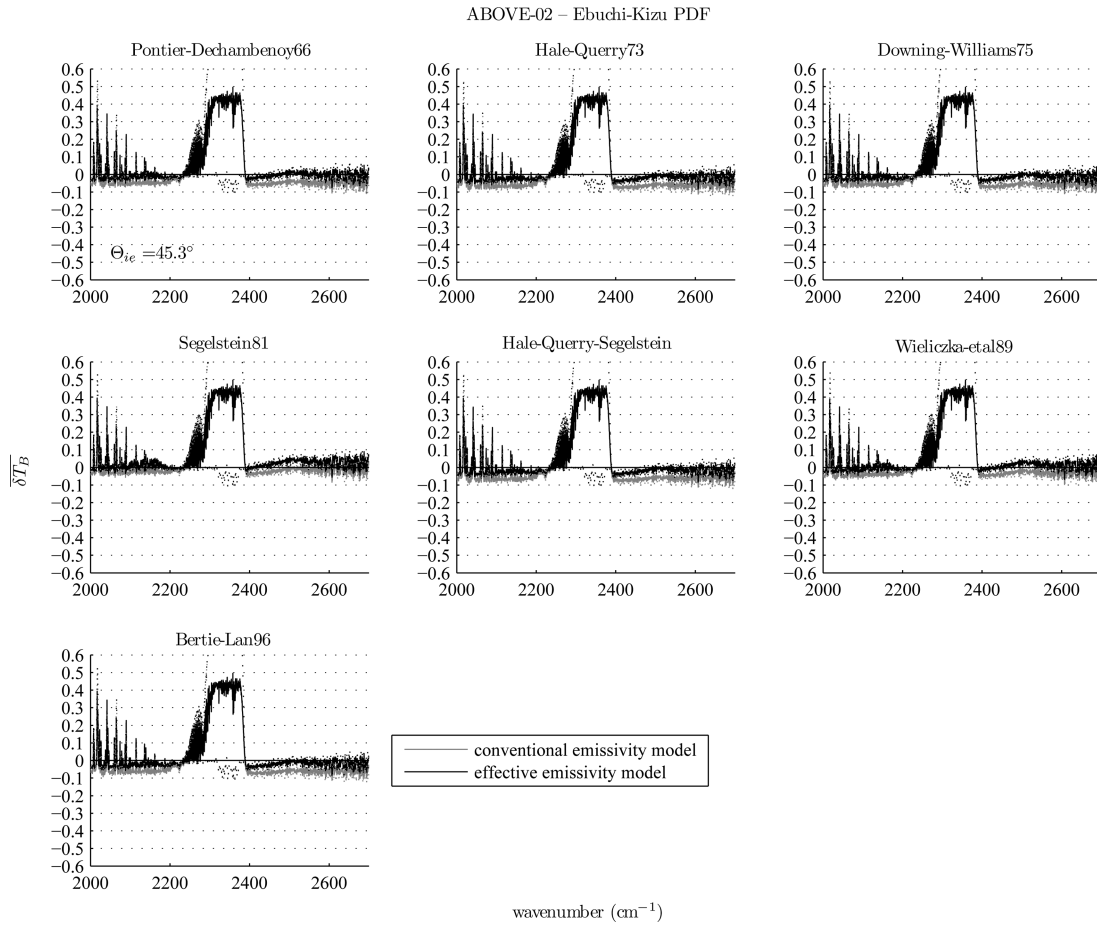


Fig. 17. As in Fig. 5, except the measurements were acquired from the BBAERI at emission angle  $\theta_0 = \theta'_0 = 45^\circ$  from the COVE site ( $h = 23$  m) during ABOVE 2002. The IQR of daily means are shown as dotted lines (rather than dashed) to reduce clutter about the mean results.

field. Most obvious and easy to explain are the deviations arising from the latter of these. Using Line-by-Line Radiative Transfer Model calculations to simulate the effect of an unaccounted atmospheric layer between the sensor and surface (as in Subsection 4.C.4), we are able to confirm the following observed phenomena:

1. Large positive calc – obs (e.g., the spikes at the extremes of the LWIR window) occur in opaque spectral regions when the skin SST is warmer than the ambient air temperature (this was typically the case during the M-AERI campaigns), leading to net absorption within  $H_2O$  lines, as well as the  $CO_2$  and  $H_2O$  absorption bands. Likewise, the opposite occurs (negative calc – obs) when there is a temperature inversion, as was often the case during ABOVE 2003 (not shown).

2. Depressed or negative calc – obs within the semiopaque 750–830  $cm^{-1}$  band results from the increasing downwelling emission of the layer (which is not measured by the M-AERI and BBAERI uplooking views) coupled with rapidly increasing reflectivity toward smaller wavenumbers beyond the emissivity peak around 900  $cm^{-1}$ . Higher emissivity and atmospheric transmittance in the window on the

shortwave side of 900  $cm^{-1}$  renders the reflected layer emission a negligible contribution. Because this effect is not the result of path attenuation, it is manifested as a spectral depression in the calc – obs (theoretically negative, assuming it is the only source of error), regardless of the temperature profile in the layer (although it is enhanced with inversions). It is evident to varying degrees in our field data sets, but most clearly in Figs. 6 and 7.

The remaining calc – obs spectral variations are believed to result from deviations of the true refractive indices from the published values. Specifically, a pronounced, concave-down positive deviation manifests itself in the colder data sets roughly between 800 and 900  $cm^{-1}$  (see Figs. 8–10), but effectively vanishes in the warmer data sets. This temperature-dependent feature has also been observed (as emissivity, not SLR) by Hanafin and Minnett [5] and Newman *et al.* [37]. We find that the Newman *et al.* temperature-dependent data set smooths this feature out somewhat (Figs. 8–10, bottom center), although a negative bias otherwise persists throughout the LWIR window. We also find that the Bertie and Lan [32] data set mitigates this spectral feature in these colder data sets, but unfortunately

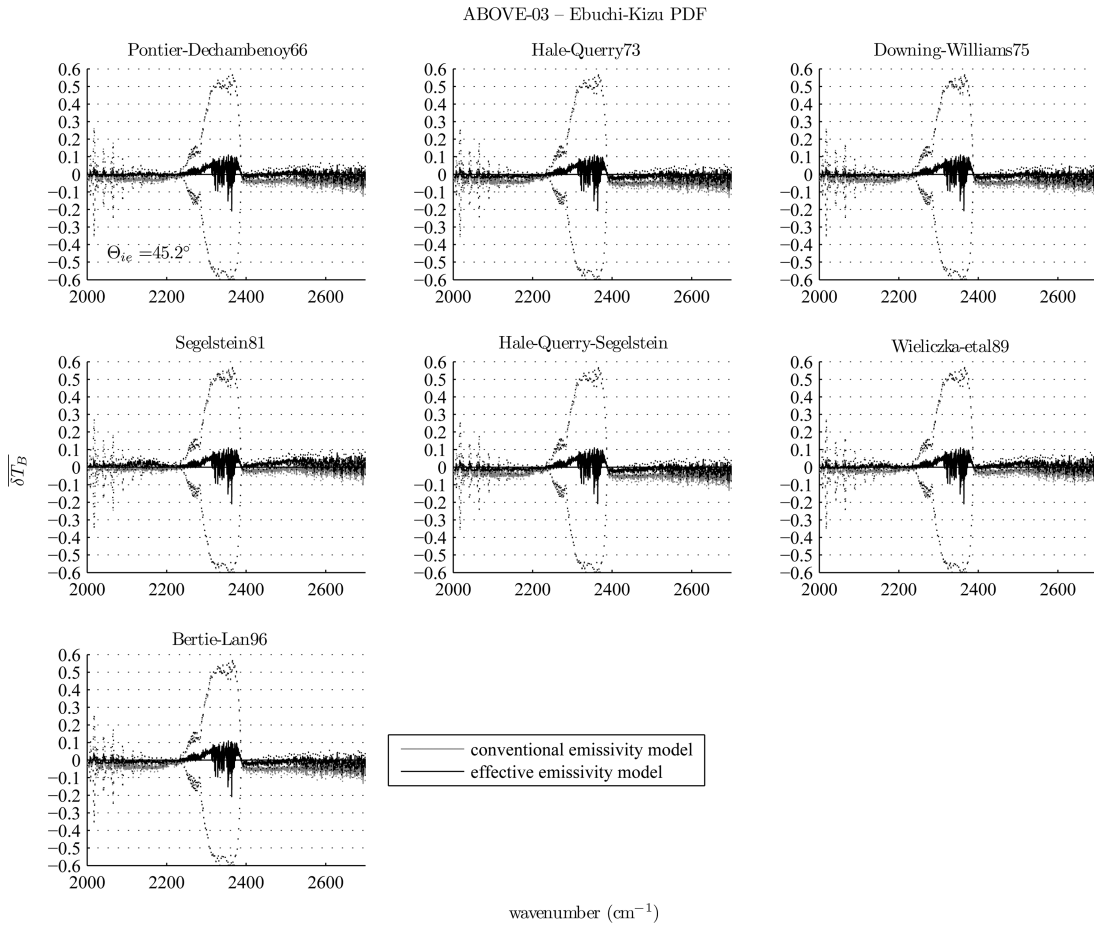


Fig. 18. As in Fig. 17, except during ABOVE 2003. Note that the IQR in the CO<sub>2</sub> absorption band ( $\approx 1.1$  K) is nearly symmetrical about zero, the lower quartile resulting from cases with surface layer temperature inversions passing QA.

introduces large negative bias in the warmer data sets (this was also observed by Newman *et al.* [37]).

Based on our results, it is difficult to make a statement as to which set of refractive indices yields the best overall agreement with field measurements (considering both the LWIR and SWIR, as well as the range of water temperatures), although the Hale and Querry [28] and Downing and Williams [29] data appear to be reasonable choices at moderate to warm temperatures. Although the work by Newman *et al.* [37] is an important start, the results here indicate that more work may be necessary to derive an optimal seawater  $N_v$  data set (i.e., one that adequately captures both the observed temperature and wavenumber dependence) for hyperspectral remote sensing applications requiring high accuracy.

#### D. Statistical Summary and Discussion

Tables 1–5 provide a condensed statistical summary of the results derived from all the campaigns. Table 1 summarizes the data samples. Tables 2 and 3 tabulate the spectral mean calc – obs,  $\delta\bar{T}_B$ , for selected window bands in the LWIR and SWIR regions, respectively. Table 4 shows the results of a paired  $t$  test for all the campaign data, and Table 5 gives the 95% confidence intervals for the  $\delta\bar{T}_B$  obtained from each model (both grouped by emission angle and spectral

window). For the LWIR, two microwindows (i.e., regions between H<sub>2</sub>O absorption lines) were selected, one on each side of the O<sub>3</sub> band (980–996 and 1123–1132 cm<sup>-1</sup>), these being subject to the least amount of continuum absorption. This selection serves to minimize any path absorption or emission occurring between the M-AERI and the surface. The SWIR windows, on the other hand, are already highly transparent (thus mitigating the need to find microwindows), but when measured from M-AERI or BBAERI the radiances typically suffer from a relatively large degree of spectral random noise. Therefore, to minimize noise, the entire 2400–2700 cm<sup>-1</sup> narrowband range was selected.

Considering first the LWIR results (Table 2, both models), we again note that  $\delta\bar{T}_B$  range can vary by a significant amount, depending on the choice of refractive indices, in these microwindow channels. As seen earlier (e.g., Fig. 2), the S81 [30] data are somewhat offset from the others by  $\approx +0.05$ –0.1 K. In a similar vein, the N05 [37] data (Table 2, bottom half) are also offset from the others, but negatively so, by  $\approx -0.05$ –0.1 K. The difference between the S81 [30] and the N05 [37] temperature-dependent data consequently reaches as much as 0.2 K, which is the same as the order of bias. As stated earlier, it is

**Table 2. Campaign Mean calc–obs for LWIR Microwindows (980–996, 1123–1132 cm<sup>-1</sup>)<sup>a</sup>**

Campaign	$\delta\bar{T}_B$ , K (for published $N_\nu$ )						
	PD66	HQ73	DW75	S81	W89	BL96	N05
Conventional Emissivity SLR Model							
AEROSE-I	-0.20	-0.22	-0.21	-0.11	-0.18	-0.19	—
AEROSE-II	-0.30	-0.32	-0.31	-0.21	-0.28	-0.29	—
EAT	-0.21	-0.24	-0.23	-0.13	-0.19	-0.21	—
ACE-Asia	-0.14	-0.17	-0.16	-0.04	-0.12	-0.13	—
SAGE	-0.12	-0.15	-0.13	-0.04	-0.10	-0.11	—
CASES	-0.17	-0.18	-0.18	-0.12	-0.16	-0.16	—
CSP (45°)	-0.10	-0.12	-0.11	-0.04	-0.09	-0.10	—
CSP (55°)	-0.15	-0.18	-0.17	-0.08	-0.14	-0.15	—
CSP (65°)	-0.17	-0.19	-0.18	-0.07	-0.14	-0.16	—
Effective Emissivity SLR Model							
AEROSE-I	-0.03	-0.06	-0.04	+0.05	-0.01	-0.02	-0.11
AEROSE-II	-0.14	-0.17	-0.16	-0.06	-0.13	-0.14	-0.21
EAT	-0.08	-0.10	-0.09	0.00	-0.06	-0.07	-0.16
ACE-Asia	+0.03	0.00	+0.01	+0.12	+0.05	+0.04	-0.07
SAGE	+0.03	+0.01	+0.02	+0.11	+0.05	+0.04	-0.05
CASES	-0.08	-0.10	-0.09	-0.04	-0.07	-0.08	-0.14
CSP (45°)	-0.05	-0.07	-0.06	+0.01	-0.03	-0.04	-0.10
CSP (55°)	-0.03	-0.05	-0.04	+0.05	-0.01	-0.02	-0.09
CSP (65°)	+0.05	+0.02	+0.04	+0.14	+0.07	+0.06	-0.02

<sup>a</sup> $\delta\bar{T}_B$  denotes the spectral mean calc – obs for the LWIR spectral microwindows defined by 980–996, 1123–1132 cm<sup>-1</sup> (chosen to avoid H<sub>2</sub>O lines). Instrument pointing angles were at 55°, except for CSP (as indicated). PD66, HQ73, DW75, S81, W89, BL96, and N05 refer to the published refractive indices [27–32,38] used in the model calculations.

reasonable to place more confidence in the other data sets (PD66, HQ73, DW75, W89, and BL96), based on self-consistency and reasonable agreement with our measurements. With regard to the N05 LWIR temperature-dependent data, the least negatively biased results appear to occur under the relatively cold (but still well above freezing) SST conditions ( $\simeq 10^\circ\text{C}$ – $15^\circ\text{C}$ ) encountered during ACE-Asia and SAGE. Overall, the effective emissivity SLR model provides a consistent reduction of bias of  $\simeq 0.13$ – $0.17$  K (at  $\theta_0 = 55^\circ$ ), with the exception of the polar case (i.e., CASES), which was about half this ( $\simeq 0.09$  K), probably because of the cold skin SST and reduced contrast between the atmosphere and sea surface. At the other two emission angles, 45° and 65°, the difference in bias during CSP is consistently 0.06 K and  $\simeq 0.21$ – $0.22$  K, respectively, for wind speeds  $\bar{U}_{10} \simeq 6.2 \pm 2.5 \text{ m s}^{-1}$ . With the exception of AEROSE-II (which for reasons not fully understood, has a uniformly larger negative bias; see Subsection 4.C.1) and the S81 and N05 refractive indices, the bias is consequently  $< 0.1$  K for these LWIR channels.

Turning to the SWIR results (Table 3), there is notably less divergence among the  $N_\nu$  data sets, as was stated earlier. The effective emissivity SLR model provides a consistent reduction of bias of  $\simeq 0.08$ – $0.10$  K (at  $\theta_0 = 55^\circ$ ), again with the exception of the polar case (i.e., CASES), which was  $\simeq 0.05$  K. At the 45° emission angle, the reduction of bias during both CSP and ABOVE is consistently 0.04– $0.05$  K ( $\bar{U}_{10} \simeq 5.4 \pm 2.4 \text{ m s}^{-1}$ ), and at the 65° angle (CSP only,  $\bar{U}_{10} \simeq 6.1 \pm 2.5 \text{ m s}^{-1}$ ), the difference was consistently  $\simeq 0.17$  K.

Although these numbers may appear small, they are nevertheless statistically significant given the large numbers of observations involved (see Table 1). Statistical significance at the 5% level is demonstrated using Student's *t* test, the results of which are given in Tables 4 and 5. The *t* tests are performed on the daily mean results for all the campaign data and refractive indices (omitting the Segelstein [30] and Newman *et al.* [37] data sets), each day being the mean of  $O(10^2)$  spectra. Table 4 shows a paired test that demonstrates the magnitude of correction provided by the effective emissivity SLR model along with the means and standard deviations of surface wind speed and skin SST, keeping in mind that the magnitude of correction varies directly with wind speed. Table 5 shows the 95% confidence intervals for the biases of each model. Condensing these tabulated results by considering all cases, the effective emissivity SLR provides a correction in window channels ranging between 0.04 and 0.22 K (Table 4), reducing overall biases from the range of ( $-0.19$ ,  $-0.06$ ) K to the range of ( $-0.06$ ,  $+0.08$ ) K (Table 5). While the results for  $\theta_0 = 55^\circ$  encompass a large range of wind speeds and atmospheric conditions, those for 45° and 65° were obtained under low to moderate wind speeds, and the 65° data were restricted to a tropical environment. Therefore, larger corrections may be expected under higher wind speed regimes ( $\bar{U}_{10} \gtrsim 8 \text{ m s}^{-1}$ ) of the order of those calculated in Part I (up to 0.4 K for  $\theta_0 \simeq 65^\circ$ ).

## 5. Summary and Conclusions

This paper, being the second of a two-part work, has described an extensive body of FTS (M-AERI and

Table 3. Campaign Mean calc-obs for the SWIR Narrowband Window (2400–2700 cm<sup>-1</sup>)<sup>a</sup>

Campaign	<i>PD66</i>	<i>HQ73</i>	<i>DW75</i>	<i>S81</i>	<i>W89</i>	<i>BL96</i>
Conventional Emissivity SLR Model						
AEROSE-I	-0.10	-0.11	-0.11	-0.07	-0.08	-0.11
AEROSE-II	-0.19	-0.20	-0.20	-0.16	-0.17	-0.20
EAT	-0.11	-0.12	-0.12	-0.08	-0.09	-0.12
ACE-Asia	-0.08	-0.09	-0.09	-0.05	-0.07	-0.09
SAGE	-0.08	-0.09	-0.09	-0.05	-0.06	-0.09
CASES	-0.15	-0.15	-0.15	-0.13	-0.14	-0.15
CSP (45°)	-0.08	-0.09	-0.09	-0.05	-0.07	-0.09
CSP (55°)	-0.11	-0.12	-0.12	-0.08	-0.09	-0.12
CSP (65°)	-0.09	-0.11	-0.10	-0.05	-0.07	-0.11
ABOVE-02 (45°)	-0.05	-0.07	-0.06	-0.02	-0.04	-0.07
ABOVE-03 (45°)	-0.04	-0.05	-0.05	-0.02	-0.03	-0.05
Effective Emissivity SLR Model						
AEROSE-I	0.00	-0.01	-0.01	+0.03	+0.02	-0.01
AEROSE-II	-0.09	-0.10	-0.10	-0.06	-0.07	-0.10
EAT	-0.03	-0.04	-0.04	0.00	-0.02	-0.04
ACE-Asia	+0.01	0.00	0.00	+0.04	+0.02	0.00
SAGE	+0.01	0.00	+0.01	+0.04	+0.03	0.00
CASES	-0.10	-0.10	-0.10	-0.08	-0.09	-0.10
CSP (45°)	-0.04	-0.05	-0.05	-0.01	-0.03	-0.05
CSP (55°)	-0.01	-0.03	-0.03	+0.02	0.00	-0.03
CSP (65°)	+0.08	+0.06	+0.06	+0.11	+0.09	+0.06
ABOVE-02 (45°)	-0.01	-0.02	-0.02	+0.02	+0.01	-0.02
ABOVE-03 (45°)	-0.01	-0.02	-0.02	+0.01	0.00	-0.02

<sup>a</sup>Similar to Table 2, except for the highly transparent SWIR narrowband window defined by 2400–2700 cm<sup>-1</sup>. A narrow band was chosen, as opposed to a microwindow, to minimize FTS SWIR spectral random noise. Instrument pointing angles were at 55°, except for CSP and ABOVE (as indicated). Note that *N05* [36] refractive indices are not available for SWIR channels.

BBAERI) spectral radiance measurements that has served to validate a simplified surface-leaving radiance (SLR) model derived in Part I [6]. As detailed in the first paper, the new model was developed to attain better agreement with observations by treating both emissivity and atmospheric reflection in a systematic, yet relatively simple, manner. The field data used in this work were obtained under a range of climatological conditions, including tropical, midlatitude, and maritime-polar regional samples. Furthermore, these data were not restricted to clear skies only, but included nonprecipitating clouds as well as dust aerosols during significant outflow events.

The effective emissivity SLR model was shown to provide a consistent spectral reduction of bias over the conventional model. Although the magnitude of correction varies throughout the spectrum, the bias difference in transparent LWIR microwindows (980–996, 1123–1132 cm<sup>-1</sup>) was of the order of  $\Delta T_B \simeq 0.05$  K,  $\simeq 0.15$  K, and  $\simeq 0.21$  K for emission angles 45°, 55°, and 65°, respectively. In the SWIR narrowband window (2400–2700 cm<sup>-1</sup>), the bias difference was of the order of  $\simeq 0.04$  K,  $\simeq 0.09$  K and  $\simeq 0.16$  K for these emission angles. Although this correction in modeled SLR may appear small, it nevertheless amounts to a significant improvement

Table 4. Statistical Summary Grouped by  $\theta_0$  and Spectral Region<sup>a</sup>

$\theta_0$	Window	Wind Speed		Skin SST		Paired <i>t</i> Test					
		$\bar{U}_{10}$	$\sigma$	$\bar{T}_s$	$\sigma$	$H_0$	<i>t</i>	DF	<i>p</i>	95% CI	
										Lower	Upper
45°	LWIR	6.2	2.5	28.9	1.2	reject	43	134	0.00	0.05	0.06
55°	LWIR	7.0	3.0	19.8	8.4	reject	83	794	0.00	0.15	0.15
65°	LWIR	6.2	2.5	28.9	1.2	reject	62	134	0.00	0.21	0.22
45°	SWIR	5.4	2.4	26.4	2.9	reject	68	229	0.00	0.04	0.04
55°	SWIR	7.0	3.3	19.7	8.5	reject	100	739	0.00	0.09	0.09
65°	SWIR	6.1	2.7	28.8	1.2	reject	92	119	0.00	0.16	0.17

<sup>a</sup>Paired Student's *t* test for the difference in daily mean calc – obs resulting from the two SLR models for all campaign data and five published refractive indices [27–29,31,32] (omitting *S81* [30] and *N05* [38]) grouped by emission angle and spectral window;  $H_0 : \mu = 0$  at the 5% significance level, *t* denotes the test statistic, DF is the degrees of freedom ( $5 \times N - 1$ ), *p* is the probability of surpassing *t* under  $H_0$ , and CI is the 95% confidence interval (defined by the upper and lower bounds). LWIR and SWIR denote the spectral windows defined in Tables 2 and 3, respectively. For reference, the means and standard deviations of the wind speed and skin SST are also given.

Table 5. Statistical Summary: 95% Confidence Intervals<sup>a</sup>

$\theta_0$	Window	95% CI			$\sigma$
		Lower	Upper		
Conventional Emissivity SLR					
45°	LWIR	-0.11	-0.10	0.04	
55°	LWIR	-0.19	-0.18	0.08	
65°	LWIR	-0.18	-0.16	0.07	
45°	SWIR	-0.08	-0.06	0.05	
55°	SWIR	-0.12	-0.11	0.06	
65°	SWIR	-0.11	-0.08	0.08	
Effective Emissivity SLR					
45°	LWIR	-0.06	-0.04	0.03	
55°	LWIR	-0.04	-0.03	0.08	
65°	LWIR	+0.04	+0.06	0.05	
45°	SWIR	-0.03	-0.02	0.04	
55°	SWIR	-0.03	-0.02	0.06	
65°	SWIR	+0.06	+0.08	0.07	

<sup>a</sup>Similar to Table 4 except showing 95% confidence intervals (CI) and standard deviation for  $\delta\bar{T}_B$  (bias) obtained from each SLR model considered individually.

in the context of the complete forward model, with larger corrections expected under wind speed regimes higher than those sampled here ( $\bar{U}_{10} \gtrsim 8 \text{ m s}^{-1}$ ), especially at the 65° emission angle. Furthermore, because of the large quantity of observations used ( $N > 150$  daily means derived from thousands of LWIR and SWIR spectra), the results were demonstrated to have statistical significance. To our knowledge, these analyses constitute the most comprehensive validation of ocean emissivity–reflection models to date.

One motivation of our use of daily means was to make this exploratory study more tractable, given the large volume of data available for this research. Our initial results, reported here, support the predictions of the new SLR model, but they also stimulate the need for further research, including the analysis of subsets of the data averaged as necessary according to ancillary variables, such as SST and cloud cover to reveal the factors that control the spectral characteristics of the calc – obs. To explore the additional information that might be gleaned by avoiding the use of daily averaged spectra as in this study, we have conducted an initial analysis of the CASES data, identifying the effects of cloud cover by using a simple cloud mask (i.e., omitting spectra with downlooking minus uplooking window channel brightness temperatures less than some positive threshold,  $\approx 30 \text{ K}$ ) and found that, among other things, the amount of correction offered by the effective emissivity model (under near-freezing conditions) is brought more into line with the results of the analyses of other campaigns (i.e., LWIR  $\Delta T_B \approx 0.15 \text{ K}$  at 55°).

This work has also provided an independent evaluation of seven different published sets of measured IR refractive indices. In agreement with other recent work on the subject [5,87], we found a significant temperature dependence, which, if unaccounted for,

can lead to spectral SLR errors of the same order of magnitude as those we have sought to correct. Therefore, additional work is desirable to derive an optimal seawater  $N_\nu$  data set (i.e., one that adequately captures both the observed temperature and wavenumber dependence) for high-accuracy hyperspectral IR remote sensing applications. Additional investigations into the dependence of SLR calc – obs (and consequently, the refractive indices) on temperature will be the subject of future research.

## Appendix A: Acronyms

ABOVE, AIRS BBAERI Ocean Validation Experiment (2002, 2003)

ACE, Asia-Asian Pacific Regional Aerosol Characterization Experiment (2001)

AERI, Atmospheric Emitted Radiance Interferometer

AEROSE, Aerosol and Ocean Science Expeditions (2004, 2006)

AIRS, Atmospheric Infrared Sounder

AMMA, African Monsoon Multidisciplinary Analysis (2006)

BBAERI, Baltimore-Bomem AERI

CASES, Canadian Arctic Shelf Exchange Study (2003)

COVE, Ocean Validation Experiment

CSP, Combined Sensor Program (1996)

EAT, East Atlantic Transect (1999)

FOV, field of view

FTS, Fourier transform spectrometer

IQR, interquartile range

LUT, lookup table

LWIR, longwave infrared

M-AERI, Marine AERI

NH, Northern Hemisphere

PDF, probability density function

QA, quality assurance

SAGE, Surface–Ocean Lower-Atmosphere Studies Air-Sea Gas Exchange Experiment (2004)

SLR, surface-leaving radiance

SST, sea surface temperature

SWIR, shortwave infrared

This work was supported by the Joint Center for Satellite Data Assimilation (JCSDA) FY05-06 Science Development and Implementation Task (JSDI, J. Yoe and J. Le Marshall) and the NESDIS/STAR Satellite Meteorology and Climatology Division. We thank C. Barnet (NESDIS/STAR task monitor) and C. Dean (PSGS program manager) for their support of this project. NASA funded the development of the M-AERI through contract NAS5-31361 along with several of the research cruises (NNG04HZ33C); the U.S. National Science Foundation (NSF) supported the SAGE cruise (OCE 0327188), and the Atmospheric Radiation Measurement (ARM) program of the U.S. Department of Energy contributed to the CSP cruise. The AEROSE campaigns have been supported by the Howard

University NOAA Center for Atmospheric Sciences through the Educational Partnership Program's Minority Serving Institutions Program, NSF Grant ATM-9703167 and NASA Grant NG-1224. We also extend our thanks to B. Howell (University of Wisconsin—Madison) for providing us with AERI to NetCDF conversion software, two reviewers who provided constructive feedback, and P. Clemente-Colón, M. Szczodrak, M. Izaguirre, W. L. Smith, R. Knuteson, B. Osborne along with others too numerous to mention here who contributed to the success of many FTS field campaigns conducted over the past decade. The views, opinions, and findings contained in this report are those of the authors and should not be construed as an official National Oceanic and Atmospheric Administration or U.S. Government position, policy, or decision.

## References

1. W. L. Smith, R. O. Knuteson, H. E. Revercomb, W. Feltz, H. B. Howell, W. P. Menzel, N. R. Nalli, O. Brown, J. Brown, P. Minnett, and W. McKeown, "Observations of the infrared properties of the ocean: implications for the measurement of sea surface temperature via satellite remote sensing," *Bull. Am. Meteorol. Soc.* **77**, 41–51 (1996).
2. P. J. Minnett, R. O. Knuteson, F. A. Best, B. J. Osborne, J. A. Hanafin, and O. B. Brown, "The Marine-Atmospheric Emitted Radiance Interferometer (M-AERI): a high-accuracy, sea-going infrared spectroradiometer," *J. Atmos. Ocean. Tech.* **18**, 994–1013 (2001).
3. K. Masuda, T. Takashima, and Y. Takayama, "Emissivity of pure and sea waters for the model sea surface in the infrared window regions," *Remote Sens. Environ.* **24**, 313–329 (1988).
4. P. Watts, M. Allen, and T. Nightingale, "Sea surface emission and reflection for radiometric measurements made with the along-track scanning radiometer," *J. Atmos. Ocean. Tech.* **13**, 126–141 (1996).
5. J. A. Hanafin and P. J. Minnett, "Measurements of the infrared emissivity of a wind-roughened sea surface," *Appl. Opt.* **44**, 398–411 (2005).
6. N. R. Nalli, P. J. Minnett, and P. van Delst, "Emissivity and reflection model for calculating unpolarized isotropic water surface-leaving radiance in the infrared. I: Theoretical development and calculations," *Appl. Opt.* **47**, 3701–3721 (2008).
7. K. Yoshimori, K. Itoh, and Y. Ichioka, "Thermal radiative and reflective characteristics of a wind-roughened water surface," *J. Opt. Soc. Am. A* **11**, 1886 (1994).
8. K. Yoshimori, K. Itoh, and Y. Ichioka, "Optical characteristics of a wind-roughened water surface: a two-dimensional theory," *Appl. Opt.* **34**, 6236–6247 (1995).
9. X. Wu and W. L. Smith, "Emissivity of rough sea surface for 8–13  $\mu\text{m}$ : modeling and validation," *Appl. Opt.* **36**, 1–11 (1997).
10. D. E. Freund, R. I. Joseph, D. J. Donohue, and K. T. Constantines, "Numerical computations of rough sea surface emissivity using the interaction probability density," *J. Opt. Soc. Am. A* **14**, 1836–1849 (1997).
11. J. A. Shaw and C. Marston, "Polarized infrared emissivity for a rough water surface," *Opt. Express* **7**, 375–380 (2000).
12. N. R. Nalli, W. L. Smith, and B. Huang, "Quasi-specular model for calculating the reflection of atmospheric emitted infrared radiation from a rough water surface," *Appl. Opt.* **40**, 1343–1353 (2001).
13. B. G. Henderson, J. Theiler, and P. Villeneuve, "The polarized emissivity of a wind-roughened sea surface: a Monte Carlo model," *Remote Sens. Environ.* **88**, 453–467 (2003).
14. C. Bourlier, "Unpolarized infrared emissivity with shadow from anisotropic rough sea surfaces with non-Gaussian statistics," *App. Opt.* **44**, 4335–4349 (2005).
15. C. Bourlier, "Unpolarized emissivity with shadow and multiple reflections from random rough surfaces with the geometric optics approximation: application to Gaussian sea surfaces in the infrared band," *Appl. Opt.* **45**, 6241–6254 (2006).
16. K. Masuda, "Infrared sea surface emissivity including multiple reflection effect for isotropic Gaussian slope distribution model," *Remote Sens. Environ.* **103**, 488–496 (2006).
17. K. Caillault, S. Fauqueux, C. Bourlier, P. Simoneau, and L. Labarre, "Multiresolution optical characteristics of rough sea surface in the infrared," *Appl. Opt.* **46**, 5471–5481 (2007).
18. H. E. Revercomb, H. Buijs, H. B. Howell, D. D. LaPorte, W. L. Smith, and L. A. Stromovsky, "Radiometric calibration of IR Fourier transform spectrometers: solution to a problem with the high-resolution interferometer sounder," *Appl. Opt.* **27**, 3210–3218 (1988).
19. M. J. Post, C. W. Fairall, J. B. Snider, Y. Han, A. B. White, W. L. Ecklund, K. M. Weickmann, P. K. Quinn, D. I. Cooper, S. M. Sekelsky, R. E. McIntosh, P. Minnett, and R. O. Knuteson, "The Combined Sensor Program: an air-sea science mission in the central and western Pacific Ocean," *Bull. Am. Meteorol. Soc.* **78** (12), 2797–2815 (1997).
20. J. H. Seinfeld, G. R. Carmichael, R. Arimoto, W. C. Conant, F. J. Brechtel, T. S. Bates, T. A. Cahill, A. D. Clarke, S. J. Doherty, P. J. Flatau, J. K. B. J. Huebert, K. M. Markowicz, P. K. Quinn, L. M. Russell, P. B. Russell, A. Shimizu, Y. Shinozuka, C. H. Song, Y. Tang, I. Uno, A. M. Vogelmann, R. J. Weber, J.-H. Woo, and X. Y. Zhang, "ACE-ASIA: regional climatic and atmospheric chemical effects of asian dust and pollution," *Bull. Am. Meteorol. Soc.* **85**, 367–380 (2004).
21. N. R. Nalli, P. Clemente-Colón, P. J. Minnett, M. Szczodrak, V. Morris, E. Joseph, M. D. Goldberg, C. Barnet, W. W. Wolf, A. Jessup, R. Branch, R. O. Knuteson, and W. F. Feltz, "Ship-based measurements for infrared sensor validation during Aerosol and Ocean Science Expedition 2004," *J. Geophys. Res.* **111**, D09S04 (2006).
22. V. Morris, P. Clemente-Colón, N. R. Nalli, E. Joseph, R. A. Armstrong, Y. Detrés, M. D. Goldberg, P. J. Minnett, and R. Lumpkin, "Measuring trans-Atlantic aerosol transport from Africa," *EOS Trans. Am. Geophys. Union* **87**, 565–571 (2006).
23. M. Harvey, C. S. Law, M. Smith, J. A. Hall, E. Abraham, C. Stevens, M. Hadfield, D. Ho, B. Ward, S. D. Archer, J. Cainey, K. Currie, M. Ellwood, P. Hill, G. Jones, J. Kuparinen, B. Macaskill, W. Main, A. Marriner, J. McGregor, C. McNeil, P. J. Minnett, S. Nodder, J. Peloquin, S. Pickmere, M. Pinkerton, K. Safi, R. Thompson, M. Walkington, S. Wright, and L. Ziolkowski, "The SOLAS Air-Sea Gas Exchange Experiment (SAGE) 2004," submitted to Deep-Sea Res. Part II.
24. W. W. McMillan, R. Hoff, L. Strow, J. Comer, K. Lightner, E. Maddy, K. McCann, M. McCourt, and K. Rutledge, "ABOVE: The BBAERI AIRS Ocean Validation Experiment," in *Optical Remote Sensing*, OSA Technical Digest (Optical Society of America, 2003), paper OTuA2, pp. 46–48.
25. C. K. Rutledge, G. L. Schuster, T. P. Charlock, F. M. Denn, W. L. Smith, Jr., B. E. Fabbri, J. J. Madigan, Jr., and R. J. Knapp, "Offshore radiation observations for climate research at the CERES Ocean Validation Experiment: a new 'laboratory' for retrieval algorithm testing," *Bull. Am. Meteorol. Soc.* **87**, 1211–1222 (2006).
26. C. C. Borel, "ARTEMIS-an algorithm to retrieve temperature and emissivity from hyper-spectral thermal image data," unclassified report LA-UR-027907 (Los Alamos National

- Laboratory, 2003), presented at 28th Annual GOMACTech Conference, 31 March 31 2003 to 3 April 2003, Hyperspectral Imaging Session.
27. L. Pontier and C. Dechambenoit, "Determination des constantes optiques de l'eau liquide entre 1 et 40 microns. Application au calcul de son pouvoir reflecteur et de son emissivite," *Ann. Geophys.* **22**, 633–641 (1966).
  28. G. M. Hale and M. R. Querry, "Optical constants of water in the 200-nm to 200- $\mu\text{m}$  wavelength region," *Appl. Opt.* **12**, 555–563 (1973).
  29. H. D. Downing and D. Williams, "Optical constants of water in the infrared," *J. Geophys. Res.* **80**, 1656–1661 (1975).
  30. D. J. Segelstein, "The complex refractive index of water," Master's thesis (University of Missouri–Kansas City, 1981).
  31. D. M. Wieliczka, S. Weng, and M. R. Querry, "Wedge shaped cell for highly absorbent liquids: infrared optical constants of water," *Appl. Opt.* **28**, 1714–1719 (1989).
  32. J. E. Bertie and Z. Lan, "Infrared intensities of liquids. XX. The intensity of the OH stretching band of liquid water revisited and the best current values of the optical constants of  $\text{H}_2\text{O}$  (l) at 25°C between 15,000 and 1  $\text{cm}^{-1}$ ," *Appl. Spectrosc.* **50**, 1047–1057 (1996).
  33. D. Friedman, "Infrared characteristics of ocean water (1.5–15  $\mu\text{m}$ )," *Appl. Opt.* **8**, 2073–2078 (1969).
  34. C. Cox and W. Munk, "Some problems in optical oceanography," *J. Mar. Res.* **14**, 63–78 (1955).
  35. C. Cox and W. Munk, "Measurements of the roughness of the sea surface from photographs of the Sun's glitter," *J. Opt. Soc. Am.* **44**, 838–850 (1954).
  36. N. Ebuchi and S. Kizu, "Probability distribution of surface wave slope derived using sun glitter images from geostationary meteorological satellite and surface vector winds from scatterometers," *J. Oceanography* **58**, 477–486 (2002).
  37. S. M. Newman, J. A. Smith, M. D. Glew, S. M. Rogers, and J. P. Taylor, "Temperature and salinity dependence of sea surface emissivity in the thermal infrared," *Q. J. R. Meteorol. Soc.* **131**, 2539–2557 (2005).
  38. C. J. Merchant, A. R. Harris, M. J. Murray, and A. M. Závody, "Toward the elimination of bias in satellite retrievals of sea surface temperature, 1, Theory, modeling and interalgorithm comparison," *J. Geophys. Res.* **104**, 23565–23578 (1999).
  39. A. Ignatov, J. Sapper, I. Laszlo, N. R. Nalli, and K. B. Kidwell, "Operational aerosol observations (AEROBS) from AVHRR/3 onboard NOAA-KLM satellites," *J. Atmos. Ocean. Tech.* **21**, 3–26 (2004).
  40. S. A. Clough, M. J. Iacono, and J. L. Moncet, "Line-by-line calculations of atmospheric fluxes and cooling rates: application to water vapor," *J. Geophys. Res.* **97**, 15761–15785 (1992).